8-7-2017

Metrology of DNA Arrays by Super-Resolution Microscopy

Christopher M. Green
Boise State University

Kelly Schutt
Boise State University

Noah Morris
Boise State Univrsity

Reza M. Zadegan
Boise State University

William L. Hughes
Boise State University

See next page for additional authors

Publication Information

Green, Christopher M.; Schutt, Kelly; Morris, Noah; Zadegan, Reza M.; Hughes, William L.; Kuang, Wan; and Graugnard, Elton. (2017). "Metrology of DNA Arrays by Super-Resolution Microscopy". *Nanoscale, 29*, 10205-10211. http://dx.doi.org/10.1039/C7NR00928C

Authors
Christopher M. Green, Kelly Schutt, Noah Morris, Reza M. Zadegan, William L. Hughes, Wan Kuang, and Elton Graugnard

Nanoscale

Paper

Metrology of DNA Arrays by Super-Resolution Microscopy†

Christopher M. Green,[a] Kelly Schutt,[a] Noah Morris,[b] Reza Zadegan,[b] William L. Hughes,[a] Wan Kuang,[b]* and Elton Graugnard[a]*

Received 07th February 2017,
Accepted 00th January 20xx

DOI: 10.1039/x0xx00000x

www.rsc.org/

Recent results in the assembly of DNA into structures and arrays with nanoscale features and patterns have opened the possibility of using DNA for sub-10 nm lithographic patterning of semiconductor devices. Super-resolution microscopy is being actively developed for DNA-based imaging and is compatible with inline optical metrology techniques for high volume manufacturing. Here, we combine DNA tile assembly with state-dependent super-resolution microscopy to introduce crystal-PAINT as a novel approach for metrology of DNA arrays. Using this approach, we demonstrate optical imaging and characterization of DNA arrays revealing grain boundaries and the temperature dependence of array quality. For finite arrays, analysis of crystal-PAINT images provides further quantitative information of array properties. This metrology approach enables defect detection and classification and facilitates statistical analysis of self-assembled DNA nanostructures.

Introduction

As the costs and challenges of semiconductor device scaling increase,[1] new materials and technologies that enable precise patterning and placement of nanostructures are sought to supplement or replace current photolithography techniques.[2] For example, nanoscale patterning through directed self-assembly of block-copolymer (BCP) structures has been acknowledged as a viable and inexpensive lithographic mask via the International Technology Roadmap for Semiconductor manufacturing.[3,4] While progress has been made in the precise control of BCP self-assembly, defect densities and directed self-assembly of complex patterns remain challenges for manufacturing.[5] As an alternative technology, the potential for programmable, long-range order through self-assembly makes DNA an attractive material for bottom-up fabrication of nanoscale patterns,[6] as well as for templated-assembly of electronic and photonic devices with nanometer precision.[7-10]

Within the last two decades, DNA-based techniques such as origami,[6] tiles,[9] and bricks[11] have demonstrated precise control over the size, shape, arrangement, and assembly of DNA nanostructures and nanocomponents. While much work is still needed to approach commercial viability, lithographically confined DNA origami and large crystalline arrays of DNA origami show potential as self-assembled lithographic masks[12] and templates for precise nanoparticle assemblies.[13-18] As a result of these advances, the Semiconductor Research Corporation recently listed DNA-controlled sub-10 nm manufacturing as a technical area for its future roadmap.[19]

Beyond the ability to pattern at the nanoscale, metrology of patterned structures is a crucial capability in semiconductor device manufacturing that poses increasing challenges (e.g., cost, throughput, accuracy) as the device dimensions decrease.[20,21] For example, locating dislocations within a nanoscale BCP pattern requires tedious inspection of high-resolution scanning electron micrographs. Likewise, common high-resolution imaging techniques used for characterization of DNA nanostructures, such as atomic force microscopy (AFM) and transmission electron microscopy (TEM), cannot accommodate high throughput characterization. Currently, few studies have focused on developing DNA nanostructure characterization techniques that meet the demands of commercial manufacturing.[22-25] Super-resolution fluorescence microscopy has proven to be a powerful tool for biological imaging, and in the case of DNA-based nanostructures, the technique known as DNA-PAINT enables non-destructive, multiplexed optical imaging with resolution down to ~5 nm.[26-29] Based on conventional optical microscopy, super-resolution offers the potential for inline optical metrology of DNA nanostructures, a capability crucial for manufacturing.

[a] Micron School of Materials Science & Engineering, Boise State University, Boise, ID 83725, USA. E-mail: eltongraugnard@boisestate.edu; Fax: +1-208-426-4466; Tel: +1-208-426-4026.
[b] Department of Electrical & Computer Engineering, Boise State University, Boise, ID 83725, USA. E-mail: wankuang@boisestate.edu.

†Electronic supplementary information (ESI) available. See DOI: 10.1039/x0xx00000x

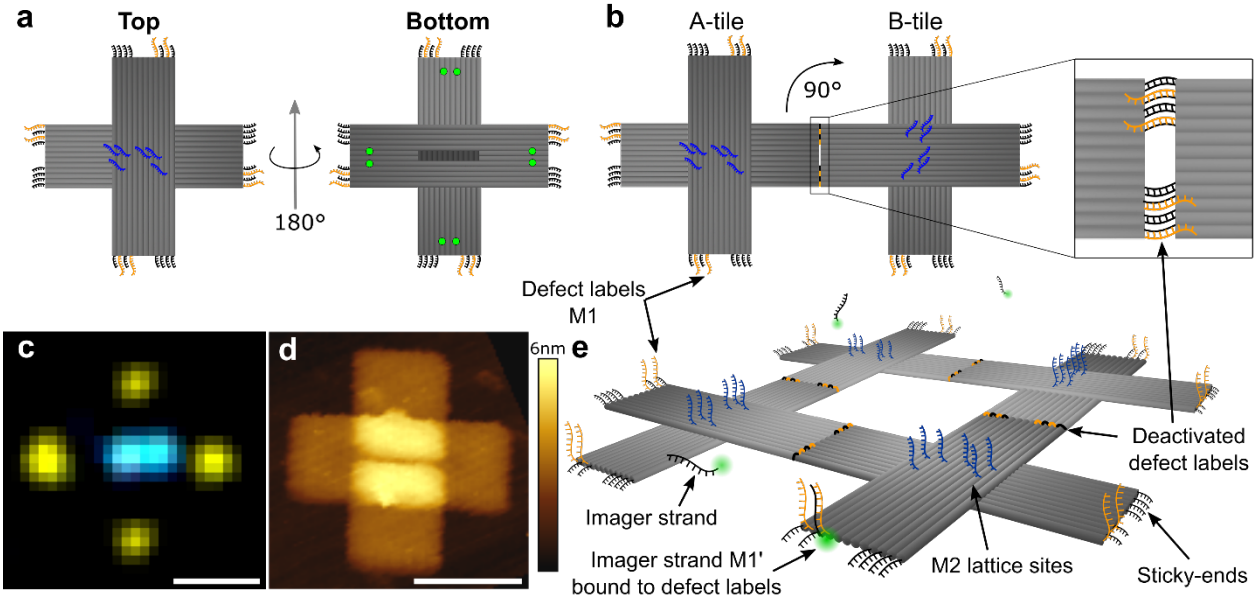

Figure 1. (a) Schematic depicting the cross-shaped DNA origami tiles used for Xtal-PAINT. Each set of sticky-ends on tile arms contain two 8 nucleotide (nt) defect labels (orange strands, M1) and six 5 nt sticky-ends (black strands). Six 8 nt docking sites extend from the center of the top of each tile (blue strands, M2). The lattice sites are aligned parallel to the central indent of the tile to delineate individual tile orientation for Xtal-PAINT imaging. Two biotinylated strands extend from the bottom of each tile arm (green circles) for immobilization to avidin-functionalized glass substrates. **(b)** Schematic of ideal sticky-end hybridization between A and B tiles. Bound tiles within an array are rotated 90° relative to neighboring tiles, which can be observed by the orientation of the lattice sites in Xtal-PAINT images. As shown in the magnified view of hybridization between A and B tile sticky-ends, all but 3 nt of the defect labels are bound, deactivating the strands as docking sites. **(c)** Xtal-PAINT and **(d)** AFM images of individual tiles corresponding to the tile schematics in **(a)**. Scale bars, 50 nm. **(e)** Schematic of a 2x2-tile array depicting imager strand docking to unbound defect labels.

Experimental

Crystal-PAINT Imaging

As a proof-of-principle of the ability to incorporate defect metrology with DNA-based patterning, we report a two-step super-resolution methodology for characterizing the periodic structure and quality of two-dimensional (2D) DNA origami arrays. We demonstrate the ability to perform defect characterization by integrating DNA-PAINT docking sites with sticky-end hybridization strands, creating state-dependent docking sites that deactivate when bound in an array. In this way, information on the state of each tile arm (deactivated/bound or active/unbound) is acquired in parallel with spatial information during imaging. Furthermore, we incorporate docking sites near the center of individual structures for characterization of array periodicity, thereby enabling step-wise characterization of the crystalline structure and single defect identification – a technique that will be referred to as crystal-PAINT characterization (Xtal-PAINT).[28] Using this technique, we reconstruct arrays of cross-shaped DNA origami tiles and identify grain boundaries occurring between arrays. In addition, utilizing statistical methods, we quantify the dimensions and size distributions of tile arrays and identify tile curvature and twist due to stress in the structure.

For DNA nanostructure assemblies formed by hybridization, binding of DNA origami tiles is dependent on unique sets of short, single-stranded DNA "sticky-ends" extended from the DNA origami tiles, as illustrated in Figure 1. Array growth is promoted through hybridization of structures with complementary sticky-end sets.[14] DNA-PAINT provides a convenient method for detecting hybridization defects between individual structures bound through sticky-end interactions. For DNA-PAINT, oligomers are extended from DNA origami tiles to provide short, single-stranded DNA "docking sites" to which complementary, fluorophore-labeled DNA "imager strands" can transiently hybridize.[27] To enable super-resolution imaging of array defects, we combine origami sticky-ends with DNA-PAINT docking sites, and this is the basis for defect identification with Xtal-PAINT. To implement Xtal-PAINT, a subset of sticky-ends were modified to facilitate either DNA-PAINT or sticky-end hybridization (M1, orange strands in Fig. 1). Modified sticky-ends (defect labels) retain the ability to hybridize for array formation but also serve as docking sites until such binding occurs. Upon binding to another origami, defect labels hybridize to complementary sticky-ends and are in a bound state and deactivated to DNA-PAINT imaging (Fig. 1b,e). Thus, defect labels are in unbound and active state at defects within an array (e.g., missing tiles) and at array boundaries. For array lattice imaging, docking sites (M2, blue strands in Fig. 1) extend from the center of each tile in a specific pattern to delineate the directionality of the cross-tile, as seen in Figure 1. Biotinylated strands have been incorporated onto the bottom of the tiles for binding to substrates functionalized with avidin binding sites (ESI Fig. S1).[30] Figure 1c shows a super-resolution image of an A-tile, where the defect labels (pseudo-colored, yellow) and lattice sites (pseudo-colored, blue) were imaged with two-color imaging, discussed below. The image clearly demonstrates the ability to resolve the ends of the origami arms and to determine the orientation of the origami. For comparison,

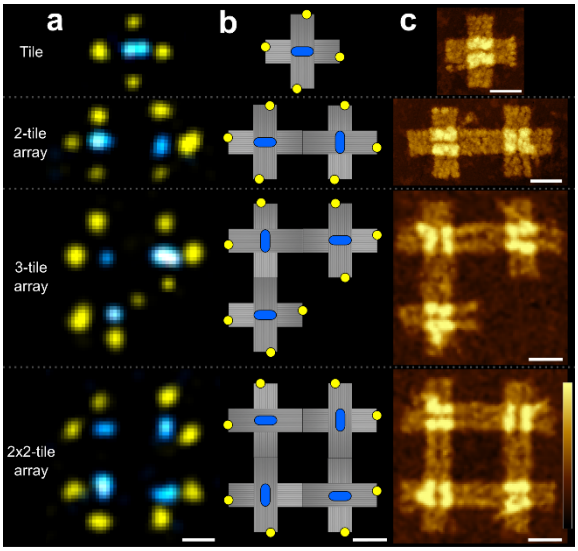

Figure 2. (a) Xtal-PAINT images of a single tile, 2-tile array, 3-tile array, and 2x2-tile array immobilized on glass by protein binding, with lattice sites (blue) and defect labels (yellow). **(b)** Schematics of the tiles and arrays deduced from the corresponding Xtal-PAINT images in **(a)** with defect labels (yellow) and lattice sites (blue). **(c)** AFM height images of tiles and arrays on mica, analogous to the structures depicted in **(a)**. Scale bars, 50 nm. AFM height scale bar, 4 nm.

Figure 1d shows an atomic force microscope (AFM) height image of an individual A tile imaged in fluid on mica. All materials and methods are described in detail in the ESI.

Results and Discussion

2x2-Tile Array Imaging

To validate Xtal-PAINT, imaging was initially performed on individual tiles and self-limiting 2x2-tile arrays (ESI Figs S2-4). The 2x2-tile arrays were constrained by replacing two adjacent sticky-end sets from A and B tiles with inert poly-thymine extensions (ESI Fig. S4). Arrays were formed in solution by constant temperature annealing and immediately deposited in a fluid well for Xtal-PAINT and on mica for AFM imaging. Super-resolution imaging of defect labels and lattice sites was performed in two steps by Exchange-PAINT,[28] a technique for multiplexed DNA-PAINT that eliminates the need for spectrally distinct imaging probes. Two distinct Cy3b-labeled imager strands (M1' and M2'), complementary to the defect labels (M1) and lattice sites (M2), respectively, were introduced to the fluid well separately for imaging (ESI Fig. S2). In Figure 2a, Xtal-PAINT images of structures progressing from individual origami tiles to self-limited 2x2-tile arrays are shown. Using spatial and state-dependent information from individual structures in Xtal-PAINT images, tiles and arrays were deduced (Fig. 2b) and compared to AFM images of analogous structures on mica (Fig. 2c). Tile arrays reconstructed from Xtal-PAINT

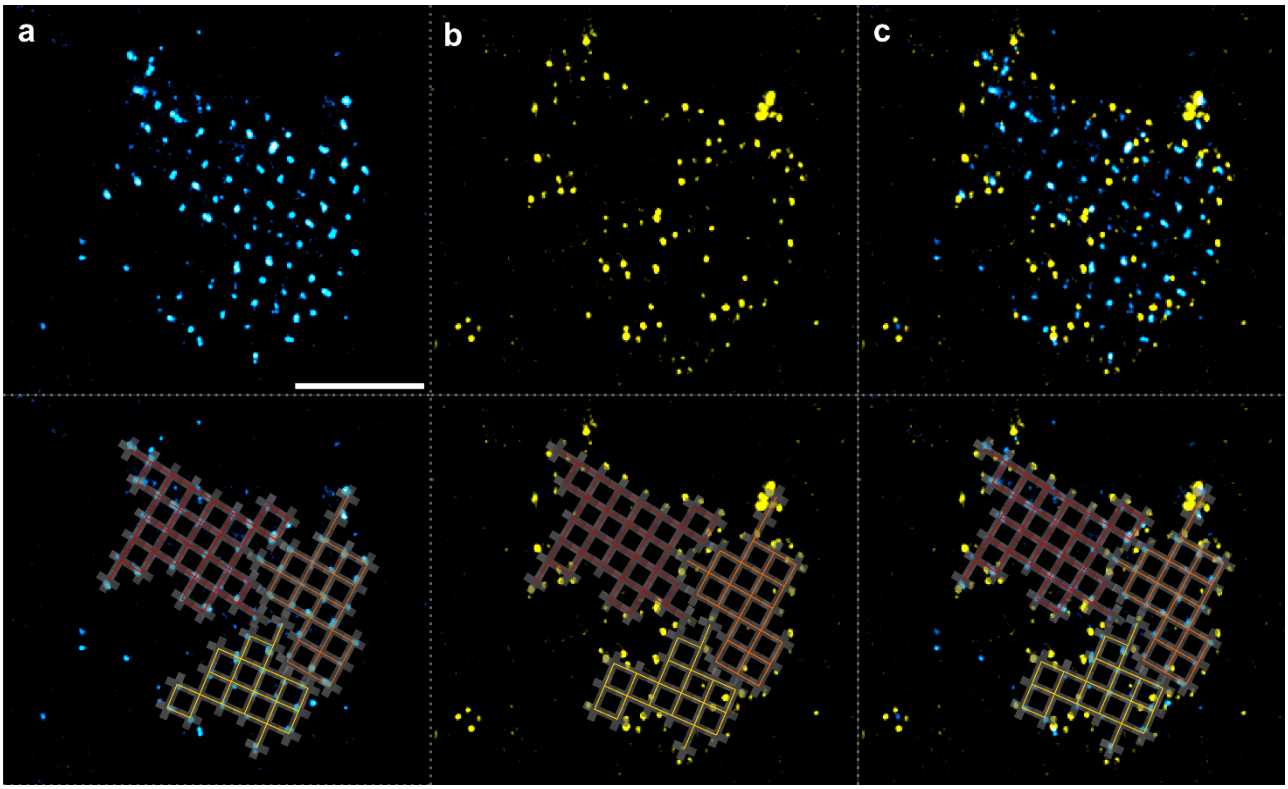

Figure 3. Xtal-PAINT image of an unbounded DNA origami array. **(a)** Image of lattice sites revealing the array periodicity, **(b)** defect label image revealing the array perimeter and missing tiles, and **(c)** combined images of a tile array resolved by Xtal-PAINT. Slight misalignment of the lattices in the arrays results in grain boundaries in the defect label image, suggesting that the large array coalesced from smaller tile arrays. Tile array models were deduced from the Xtal-PAINT images and overlaid on the images in the lower half of the figure. Lattice misalignment and grain boundaries are accounted for by modeling the structure as three arrays distinguished by color (red, orange, and yellow grids). Mean localization precision for defect label and lattice images were 8.5 ± 5.0 nm and 10.4 ± 6.1 nm, respectively. Scale bar, 500 nm.

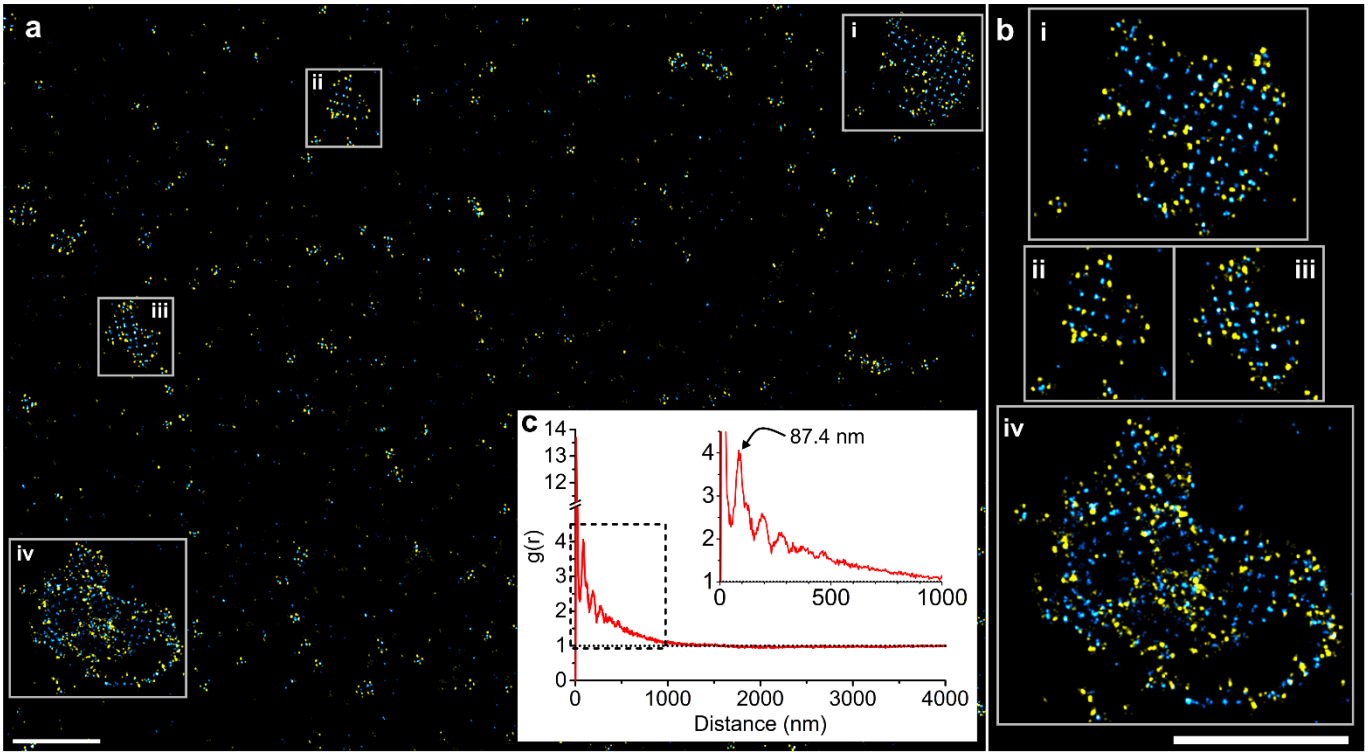

Figure 4. Xtal-PAINT image of unbounded tile arrays. **(a)** Combined defect label (yellow) and lattice (blue) images of tile arrays annealed for 24 hours near 38 °C. The four largest arrays are identified in the image by **i-iv**. **(b)** Magnified images of the tile arrays corresponding to **i-iv** in **a**. (**i**) Tile array (also shown in Figure 3) with dimensions of approximately 1 x 1 μm^2. Within the array, missing sites suggest tile vacancies. (**ii**) and (**iii**) Small tile arrays of ~ 0.5 x 0.5 μm^2 (**iv**) Large tile array that appears to extend out of the focal plane and TIRF illumination field, potentially caused by curvature induced by crystallization. **(c)** Radial distribution function of the full lattice image with peak at 87.4 nm, corresponding to the nearest neighbor distance between hybridized tiles. Higher order peaks were observed at 123 nm, 195 nm, and 275 nm, corresponding to the 2nd, 4th, and 7th nearest neighbor distances, respectively. Mean localization precision for defect label and lattice images were 8.5 ± 5.0 nm and 10.4 ± 6.1 nm, respectively. Scale bars, 1 µm.

images geometrically resemble arrays imaged by AFM on mica, and the relative orientations of lattice sites and defect labels were consistent with the tile design. Defect labels were resolved on unbound tile arms and were successfully deactivated on bound arms. These data validate the Xtal-PAINT approach to imaging lattices and defects within DNA origami arrays.

Unbounded Array Imaging

To demonstrate Xtal-PAINT imaging of unconstrained arrays, tile arrays were assembled in solution and immediately deposited in a fluid well (ESI Fig. S5). Resulting two-color images for an array consisting of approximately 81 tiles are shown in Figures 3 and 4. The Xtal-PAINT images in Figure 3 reveal a distinct crystalline array that is easily identified by the periodicity of the lattice sites (blue, Fig. 3a). The yellow defect label image in Figure 3b displays a well-defined external boundary, as well as defects within the array along paths resembling boundaries between separate arrays. Closer inspection of the lattice sites in Figure 3a reveals three grains with slightly misaligned lattices that meet at the grain boundaries observed in Figure 3b. In crystallography, this type of defect is referred to as a low angle grain boundary. A polycrystalline array model was deduced from Xtal-PAINT images and overlaid on each image in the lower half of Figure 3 to aid visualization. Individual grains in the simulated array are distinguished by color. The ability to resolve grain boundaries with Xtal-PAINT demonstrates a potential application of the technique to observe and quantify nucleation and growth of DNA origami crystals.

Figure 4 shows a larger region of a Xtal-PAINT image containing the tile array analyzed in Figure 3 (labeled as i in Fig. 4). Within the image, multiple small arrays were observed, and four arrays were observed that each consisted of more than ten tiles, with upwards of 150 tiles estimated in the largest array. The largest array shows a high degree of disorder, partially resulting from the inability to relax or flatten after immobilization by protein binding to the surface (ESI Fig. S6). To characterize the average dimensions of the tiles and the extent of short and long range order for the sample, a radial distribution function, g(r), was calculated from the lattice image and plotted in Figure 4c. Several clear peaks were observed in the g(r), and individual peaks were identified by comparison to the expected dimensions of the tile and tile arrays. The first and largest peak, occurring at ~10 nm, results from the elongated pattern of lattice sites on individual tiles and provides an approximate measure of the resolution of our system, in agreement with the mean localization precision for the lattice image.[31,32] The second peak, centered at 87 nm, is the center-to-center distance between neighboring tiles. Higher order peaks were also observed at 123 nm, 195 nm,

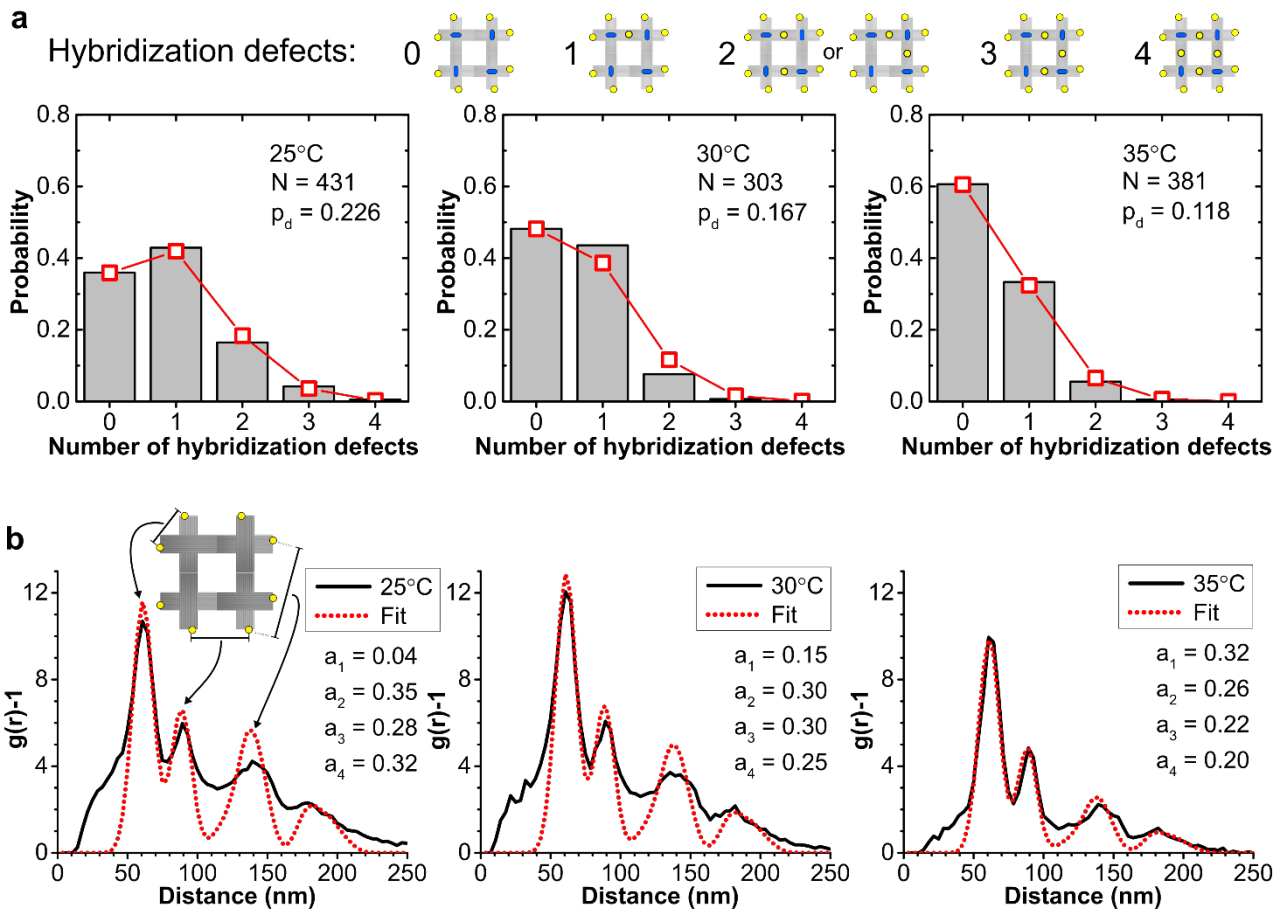

Figure 5. Quantitative analysis of 2x2-tile array defect label images. **(a)** Histograms displaying the results of hybridization defect counting for 2x2-tile arrays annealed at 25°C, 30°C, and 35°C. The legend at top indicates the structures analyzed to determine the probabilities of hybridization defects. Binomial distributions were generated from the data to calculate the probability of hybridization defects p_d for bound tile arms. p_d was observed to decrease as the temperature of anneal was increased. **(b)** Experimental and fitted g(r) for defect label images of 2x2-tile arrays annealed at 25 °C, 30 °C, and 35 °C. The first three peaks are identified with a 2x2-tile array model. The fitted g(r) were generated by spectral decomposition of the experimental distributions into a linear combination of the single tile (X_1), 2-tile array (X_2), 3-tile array (X_3), and 2x2-tile array (X_4) spectra. Fit = $a_1X_1 + a_2X_2 + a_3X_3 + a_4X_4$, where a_1-a_4 represent the fraction of tiles in each size of array out of the total number of tiles. For the fits of the 25 °C, 30 °C, and 35 °C distributions, the adjusted R-square (adj. R^2) values were 0.614, 0.722, and 0.926, respectively.

and 275 nm, corresponding to the 2nd, 4th, and 7th nearest neighbor distances, respectively (ESI Fig. S7). For reference, from AFM images the dimensions of individual tiles on mica were approximately 100 nm per side, 13 nm longer than the center-to-center spacing of tiles imaged by Xtal-PAINT in solution. This 13% difference is likely caused by out-of-plane curvature of tiles immobilized by protein-binding in the fluid cell compared to lying flat on mica; Cando analysis of the tile indicates a ~12% reduction of tile dimensions from curvature and twist, consistent with the dimensions observed in Xtal-PAINT (ESI Fig. S7).[33] The correlation length (g(r)→1) of the distribution indicates that order persists until nearly 1.6 µm, approximately equal to the largest dimension of array iv from Figure 4. The lack of distinct peaks beyond 300 nm suggests that large arrays were typically polycrystalline, consistent with the array analyzed in Figure 3. Thus, the results of Figure 4 validate the use of Xtal-PAINT in characterizing 2D crystalline DNA origami arrays. In comparison to AFM imaging, two-color Xtal-PAINT images were typically captured in ~75 minutes under conservative imaging conditions and could be expanded to capture over 10^5 µm^2 without increasing capture time, while AFM imaging of an equal area would be impractical.

Analysis of 2x2-Tile Arrays

For bounded arrays, such as the 2x2-tile array system shown in Figure 2 and ESI Figure S3, a greater depth of information can be obtained by analysis of defect label images, which reveal both hybridization defects between bound arms as well as missing or extra tiles from the finite array. To demonstrate the utility of such an analysis, a temperature dependence study was performed on the 2x2-tile array system. 2x2-tile arrays were formed by constant temperature annealing at 25 °C, 30 °C, and 35 °C for 24 hours and imaged with Xtal-PAINT. For the temperature dependence of hybridization defects, resolved 2x2-tile arrays were analyzed by counting the number of defects observed on bound arms (ESI Fig. S8). Histograms of the results are shown in Figure 5a (grey bars). The probability of hybridization defects p_d for bound tile arms was determined from the results of counting

and used to generate binomial distributions for each sample. A negative correlation was observed between p_d and the annealing temperature since annealing at higher temperatures inhibits binding between defective structures. These data provide a direct observation that annealing tiles closer to the array melting temperature (~40°C) improved array quality (ESI Fig. S9).

While hybridization defects form when docking sites fail to deactivate between bound tile arms, additional defects include missing or extra tiles within a finite array. To study the temperature dependence of the 2x2-tile array size distribution, g(r) were calculated from defect label images and are shown in Figure 5b (black). The experimental g(r) were decomposed into linear combinations of spectra for single tiles, 2-tile, 3-tile, and 2x2-tile arrays (ESI Figs S10,11). These component spectra were simulated using Monte Carlo methods using a curved and twisted tile model (ESI Fig. S10). The fitted spectra (red) are overlaid on the experimental g(r) in Figure 5b for comparison (ESI Figs S12,13). The results allow quantitative determination of the distribution of tile arrays for each sample. Overall, excellent fits were obtained when the data was modeled using a twisted origami model despite the fact that the experimental data were purely two-dimensional (focal plane). Use of three-dimensional DNA-PAINT techniques may yield additional information valuable to the analysis of array formation.[28,34,35]

The distribution of tile arrays determined by spectral decomposition (Fig. 5b) indicates that the fraction of tiles not bound in arrays increased with anneal temperature while the fraction of tiles bound within 2-tile, 3-tile, and 2x2-tile arrays decreased. The quality of fitting (indicated by adj. R^2) was also observed to increase with anneal temperature, indicating that the fraction of improperly formed arrays decreased with anneal temperature. Though the tiles were designed to form 2x2-tile arrays, larger tile structures often form due to agglomeration or out of plane hybridization (ESI Figs S4,14); such structures were not accounted for in the simulated distributions for 2x2-tile arrays and are indicated by a decrease in the quality of fitting at lower anneal temperature. These observations validate the use of statistical methods with Xtal-PAINT for quantitative and qualitative studies of DNA origami and origami arrays, and similar techniques can be developed for DNA nanostructures in general.

Conclusions

In summary, we have introduced a versatile optical metrology technique for stepwise, selective characterization of DNA arrays by means of DNA-PAINT and state-dependent docking sites. This approach revealed grain boundaries in tile arrays and provided information on the temperature dependence of array quality. Prior studies of DNA tiling have relied solely on AFM for structural characterization, but AFM imaging influences surface tiling and is not suited for large area imaging in manufacturing. While the Xtal-PAINT image in Figure 4 clearly highlights that there are challenges for creating large-scale ordered arrays with DNA origami tiles, our technique demonstrates the ability to image and quantitatively analyze these structures and gain the insight necessary to improve array formation. Xtal-PAINT provides an approach for large area, inline, defect detection and classification for DNA arrays with the statistical analysis relevant for high volume manufacturing.

Acknowledgements

We thank Bernard Yurke and Hao Chen for valuable discussions and insight, and we thank Paul Davis and Kari Livingston for assistance in AFM imaging. We thank Peng Yin for assistance with super-resolution imaging, localization software, and DNA-PAINT samples. We thank Mingjie Dai for valuable assistance. We thank Friedrich Simmel and Ali Rafat for valuable discussions and DNA origami tile samples. This work was supported by the National Science Foundation through the Scalable NanoManufacturing grant (CMMI-1344915).

References

1 M. M. Waldrop, Nature, 2016, **530**, 144–147.
2 K. Galatsis, K. L. Wang, M. Ozkan, C. S. Ozkan, Y. Huang, J. P. Chang, H. G. Monbouquette, Y. Chen, P. Nealey and Y. Botros, Adv. Mater., 2010, **22**, 769–778.
3 R. A. Segalman, Mater. Sci. Eng. R Reports, 2005, **48**, 191–226.
4 M. Neisser and S. Wurm, Adv. Opt. Technol., 2015, **4**, 235–240.
5 V. Mishra, G. H. Fredrickson and E. J. Kramer, ACS Nano, 2012, **6**, 2629–2641.
6 P. W. K. Rothemund, Nature, 2006, **440**, 297–302.
7 F. A. Aldaye, A. L. Palmer and H. F. Sleiman, Science, 2008, **321**, 1795–1799.
8 E. Winfree, F. Liu, L. A. Wenzler and N. C. Seeman, Nature, 1998, **394**, 539–44.
9 C. Lin, Y. Liu, S. Rinker and H. Yan, Chemphyschem, 2006, **7**, 1641–7.
10 E. P. Gates, A. M. Dearden and A. T. Woolley, Crit. Rev. Anal. Chem. / CRC, 2014, **44**, 354–70.
11 Y. Ke, L. L. Ong, W. M. Shih and P. Yin, Science, 2012, **338**, 1177–83.
12 C. T. Diagne, C. Brun, D. Gasparutto, X. Baillin and R. Tiron, ACS Nano, 2016, **10**, 6458–6463.
13 A. M. Hung, C. M. Micheel, L. D. Bozano, L. W. Osterbur, G. M. Wallraff and J. N. Cha, Nat. Nanotechnol., 2010, **5**, 121–6.
14 W. Liu, H. Zhong, R. Wang and N. C. Seeman, Angew. Chemie, 2011, **123**, 278–281.
15 A. Aghebat Rafat, T. Pirzer, M. B. Scheible, A. Kostina and F. C. Simmel, Angew. Chemie - Int. Ed., 2014, **53**, 7665–7668.
16 S. Woo and P. W. K. Rothemund, Nat. Commun., 2014, **5**, 4889.
17 S. P. Surwade, F. Zhou, B. Wei, W. Sun, A. Powell, C. O'Donnell, P. Yin and H. Liu, J. Am. Chem. Soc., 2013, **135**, 6778–81.
18 G. Tikhomirov, P. Petersen and L. Qian, Nat. Nanotechnol., 2017, **12**, 251–259.
19 SemiSynBio Consortium and Roadmap, 2016.

20 E. Vogel, Nat. Nanotechnol., 2007, **2**, 25–32.

21 J. A. Liddle and G. M. Gallatin, ACS Nano, 2016, **10**, 2995–3014.

22 B. Liang, A. Nagarajan, M. W. Hudoba, R. Alvarez, C. E. Castro and S. Soghrati, J. Biomech. Eng., 2017, **139**, 41003.

23 D. J. Kauert, T. Kurth, T. Liedl and R. Seidel, Nano Lett., 2011, **11**, 5558–5563.

24 I. H. Stein, V. Schüller, P. Böhm, P. Tinnefeld and T. Liedl, Chemphyschem, 2011, **12**, 689–95.

25 D. Mathur and I. L. Medintz, Anal. Chem., 2017, **89**, 2646–2663.

26 L. Schermelleh, R. Heintzmann and H. Leonhardt, J. Cell Biol., 2010, **190**, 165–175.

27 R. Jungmann, C. Steinhauer, M. Scheible, A. Kuzyk, P. Tinnefeld and F. C. Simmel, Nano Lett., 2010, **10**, 4756–61.

28 R. Jungmann, M. S. Avendaño, J. B. Woehrstein, M. Dai, W. M. Shih and P. Yin, Nat. Methods, 2014, **11**, 313–8.

29 R. Iinuma, Y. Ke, R. Jungmann, T. Schlichthaerle, J. B. Woehrstein and P. Yin, Science, 2014, **344**, 65–9.

30 J. L. Guesdon, T. Ternynck and S. Avrameas, J. Histochem. Cytochem., 1979, **27**, 1131–1139.

31 M. Ovesny, Charles University in Prague, 2016.

32 R. E. Thompson, D. R. Larson and W. W. Webb, Biophys. J., 2002, **82**, 2775–83.

33 C. E. Castro, F. Kilchherr, D.-N. Kim, E. L. Shiao, T. Wauer, P. Wortmann, M. Bathe and H. Dietz, Nat. Methods, 2011, **8**, 221–229.

34 H. P. Kao and A. S. Verkman, Biophys. J., 1994, **67**, 1291–1300.

35 B. Huang, W. Wang, M. Bates and X. Zhuang, Science, 2008, **319**, 810–3.

Electronic Supplementary Information

Metrology of DNA Arrays by Super-Resolution Microscopy

C.M. Green,[a] K. Schutt,[a] N. Morris,[b] R. Zadegan,[b] W.L. Hughes,[a] W. Kuang,[b]* and E. Graugnard[a]*

[a] Micron School of Materials Science & Engineering, Boise State University, 1910 University Drive, Boise, ID 83725
[b] Department of Electrical & Computer Engineering, Boise State University, 1910 University Drive, Boise, ID 83725

*email: wankuang@boisestate.edu and eltongraugnard@boisestate.edu

Materials and Methods

DNA origami synthesis

Single stranded M13mp18 DNA (scaffold strand) was purchased from Bayou Biolabs (Catalog # P-107) at 1.0 µg/µL in 1 x TE buffer (10 mM Tris-HCl, 1 mM EDTA, pH 8.0). Scaffold concentration was calculated to be 420 nM using the molecular weight of M13mp18/19, as reported by New England Biolabs. Staple strands were purchased unfiltered from Integrated DNA Technologies in 1 x TE buffer at 100 µM or dry and rehydrated with 1 x TE buffer to 100 µM. Biotinylated staple strands were purchased HPLC purified from Integrated DNA Technologies dry and rehydrated with 1 x TE buffer to 100 µM.

Individual cross-shaped DNA origami tiles were prepared with 10 nM scaffold strand, 50 nM body staples, and 100 nM edge staples in 0.5 x TBE buffer (44.5 mM Tris, 44.5 mM boric acid, 1 mM EDTA) with 12.5 mM $MgCl_2$. Thermal annealing was performed in an Eppendorf Mastercycler Nexus Gradient thermal cycler using the recipe reported in Table S1. After annealing, tiles were stained with 0.2 x SYBR® Gold nucleic acid gel stain and filtered by agarose gel electrophoresis (uncooled, 0.8 % Agarose, 0.5 x TBE, 8 mM $MgCl_2$) at 70 V for 2 hours. Filtered tiles were cut from the gel and retrieved by compressing the gel between glass slides.

Table S1 | Thermocycler recipe for cross-shaped DNA origami tile synthesis.

Step	Starting temp.	Cycles	ΔT per Cycle	Time per Cycle
#	(°C)	#	(°C)	(min)
1	70	1	0	15
2	70	50	-0.1	0.75
3	65	50	-0.1	0.75
4	60	50	-0.1	0.75
5	55	50	-0.1	2
6	50	50	-0.1	2
7	45	50	-0.1	2
8	40	50	-0.1	1.5
9	35	50	-0.1	1.5
10	30	20	-0.5	0.5
11	20	1	0	Hold

Tile array synthesis

Prior to mixing tiles for array formation, all tile solutions were diluted to 1 nM with TBE/Mg^{2+} buffer (0.5 x TBE, 8 mM $MgCl_2$) and annealed at 30°C for ten minutes to reduce homogenous tile interactions. Unconstrained tile arrays were assembled by mixing equal parts of A and B tiles at 1 nM in TBE/Mg^{2+} buffer and annealing for 24 hours from 38.5 to 35°C at 3 hours per 0.5°C. After annealing, unconstrained tile arrays were immediately deposited into a fluid well and onto mica (coverslip and mica heated to 35°C prior to deposition). For 2x2-tile arrays, tile polymerization was limited by replacing the sticky-ends of the R and D arms of tile A (Figure S4a) and L and D arms of tile B (Figure S4b) with inert 3 nt polyThymine (pT) extensions, leaving only the defect label strands. 2x2-tile arrays were assembled by mixing equal parts of A and B tiles at 1 nM in TBE/Mg^{2+} buffer and annealing for 24 hours at constant temperature (25, 30, or 35°C). After annealing, 2x2-tile arrays were immediately deposited onto mica, then the array solution was diluted by 4x with TBE/Mg^{2+} buffer and deposited into fluid wells.

AFM imaging

Samples for individual A and B tiles were diluted to 1 nM tiles in TBE/Mg^{2+} buffer and annealed for 10 minutes at 30°C prior to deposition on mica. After annealing, 15 µL of the tile solution was deposited onto freshly cleaved mica (see above). After 4 min, an additional 100 µL of TBE/Mg^{2+} buffer was added to the mica surface and gently removed by drawing the excess solution up with a pipette to remove any tiles in solution. This rinsing step was repeated three times. After rinsing, 80 µL of TBE/Mg^{2+} buffer with nickel (0.5 x TBE, 8 mM $MgCl_2$, 1 mM nickel (II) acetate) was deposited for imaging. AFM images of individual tiles were acquired in Peak Force Tapping mode in fluid on a Dimension Icon (Bruker) using ScanAsyst fluid probes (Bruker). Typical scanning parameters were 30 Hz scan rate, 256 lines, 1 µm x 1 µm area.

Samples for AFM imaging of unconstrained tile arrays and 2x2-tile arrays were prepared by depositing 15 µL of tile arrays at 1 nM (individual tile concentration) in TBE/Mg^{2+} buffer onto freshly cleaved mica (Ted Pella, 25 mm x 75 mm Grade V1 mica sheets, 7.8 mm punched diameter). After four minutes the solution was removed by rinsing with 4 mL DI water and dried with an N2 gun. AFM images of tile arrays were acquired in Peak Force Tapping mode in air on a MultiMode 8 (Bruker) using ScanAsyst HR probes (Bruker). Typical scanning parameters were 0.8 Hz scan rate, 1024 lines, 10 µm x 10 µm area.

Fluid well construction

Open fluid wells were constructed from treated plastic microscope slides (Ted Pella, catalog number: 260225) and Gold Seal® #1 square cover glass (Ted Pella, catalog number: 260341). A ½ in. hole was drilled into the center of the plastic microscope slide using a ½ in. glass and tile bit. For fiducial markers, 50 µL of 200 fM gold nanoparticles in methanol (Nanopartz, 150 nm silane polymer-coated spherical AuNPs, part #: E11-150-Silane-2.5 *custom order) were deposited onto the coverslip. Treated coverslips were attached to drilled microscope slides with two-part epoxy.

Fluid well sample preparation

Fluid wells were rinsed twice with 200 µL DI water, then 200 µL of 1 mg/mL biotin-labeled bovine serum albumin (Sigma-Aldrich, catalog number: A8549) in Tris/Na^+ buffer (1 x Tris-HCl, 150 mM NaCl) was deposited in the fluid well. After two minutes, the fluid well was rinsed twice with 200 µL Tris/Na^+ buffer, and 200 µL of 1mg/mL NeutrAvidin (ThermoFisher Scientific, catalog number: 31000) in Tris/Na^+ buffer was deposited in the fluid well. After two minutes, the fluid well was rinsed twice with 200 uL TBE/Mg^{2+} buffer. For unconstrained tile arrays and 2x2-tile arrays, the fluid wells were heated to the temperature of the final array annealing step for sample deposition. 200 µL of TBE/Mg^{2+} buffer was deposited in fluid wells prior to heating. For individual tile samples, fluid wells were not heated for deposition (fluid well deposition temperature ~20°C).

Before deposition into fluid wells, individual tile samples were diluted to 100 pM in TBE/Mg^{2+} buffer and 2x2-tile arrays were diluted to 250 pM in TBE/Mg^{2+} buffer. Tile or tile array solutions were deposited in the fluid well, and after two minutes the fluid well was rinsed with 200 µL of Tween-20 buffer (0.1% Tween-20, 0.5 x TBE, 18 mM $MgCl_2$). After five minutes, the fluid well was rinsed twice with 200 µL of imaging buffer (0.5 x TBE, 18 mM $MgCl_2$), then 200 µL of imaging buffer was deposited in preparation for imaging.

Optical setup

Fluorescence imaging was performed on a Nikon Eclipse TiU microscope equipped with a Nikon TIRF illuminator and a Nikon CFI Apo TIRF 100x NA 1.49 objective. An additional 1.5x magnification was used to achieve a total magnification of 150x and a pixel size of 107 nm. The area captured by our system is 55 x 55 μm^2. A 561 nm laser (Coherent Sapphire) was used for illumination with a 0.5x stop down (~8 mW TIRF illumination). A Chroma TRF49909 ET-561nm filter set was used to spectrally filter laser output. A Princeton Instruments ProEM EMCCD camera, using the imaging software LightField, was set to 25x EM gain and a data acquisition rate of 6.66 Hz. 15,000 frames were captured during each acquisition step (Figure S2). Focal drift was corrected in real time with an optical system and feedback loop developed in house.

Super-resolution Xtal-PAINT imaging

For Xtal-PAINT imaging, two imager strand solutions and one rinsing solution were prepared. Cy3b-labeled imager strands were purchased dual HPLC-filtered from Bio-Synthesis dry and rehydrated to 10 µM with 1 x TE buffer. The rinsing strand, M1*, was purchased from Integrated DNA Technologies dry and rehydrated to 100 µM with 1 x TE buffer. Imaging solution 1 consisted of Cy3b-labeled imager strand M1' diluted to 3 nM in imaging buffer (0.5x TBE, 18 mM $MgCl_2$). Imaging solution 2 consisted of Cy3b-labeled imager strand M2' diluted to 3 nM in imaging buffer. The rinsing solution consisted of rinsing strand M1* diluted to 10 nM in imaging buffer.

For two-color image acquisition, 200 µL of imaging solution 1 was first introduced to the fluid well for defect label imaging. After imaging, the fluid well was washed with the rinsing solution to remove and passivate any remaining M1' imager strands. Following rinsing, 200 uL of imaging solution 2 was introduced to the fluid well for lattice site image acquisition. Two-color image acquisition is depicted in Figure S2.

Image localization, drift correction, and image post-processing were performed with the ThunderSTORM[1] plugin for ImageJ,[2] available for download at http://zitmen.github.io/thunderstorm/. The images were filtered to remove localizations with localization uncertainty greater than 5 nm and exported at 40x magnification. Defect label images were pseudo-colored using the 'Cyan Hot' LUT available in ImageJ, and lattice site images were pseudo-colored using the 'Yellow' LUT available in ImageJ.

The localization precision for each super-resolution image was calculated as the mean uncertainty of all points localized with ThunderSTORM. ThunderSTORM calculates the uncertainty of individual localizations using a modified form of the Thompson-Larson-Webb formula.[3,4] The mean localization precision of tile array super-resolution images was less than 12 nm for all cases reported in this work.

Counting method and statistics

Self-limiting 2x2-tile array hybridization defect counting was performed using ImageJ to track the progress of counting. Hybridization defect counting was performed only on structures that could be confidently identified as 2x2-tile arrays by the presence of defect labels and lattice sites in a recognizable pattern. 2x2-tile arrays were counted by the number of defect labels resolved on bound tile arms (within the array). The number of 2x2-tile arrays counted was reported for each case; counting data is available in Table S4.

Statistical analysis with radial distribution function g(r)

The radial distribution functions of experimental and simulated images were calculated using the 'Radial Distribution Function' plugin for ImageJ which is accessible at http://imagejdocu.tudor.lu/doku.php?id=macro:radial_distribution_function.

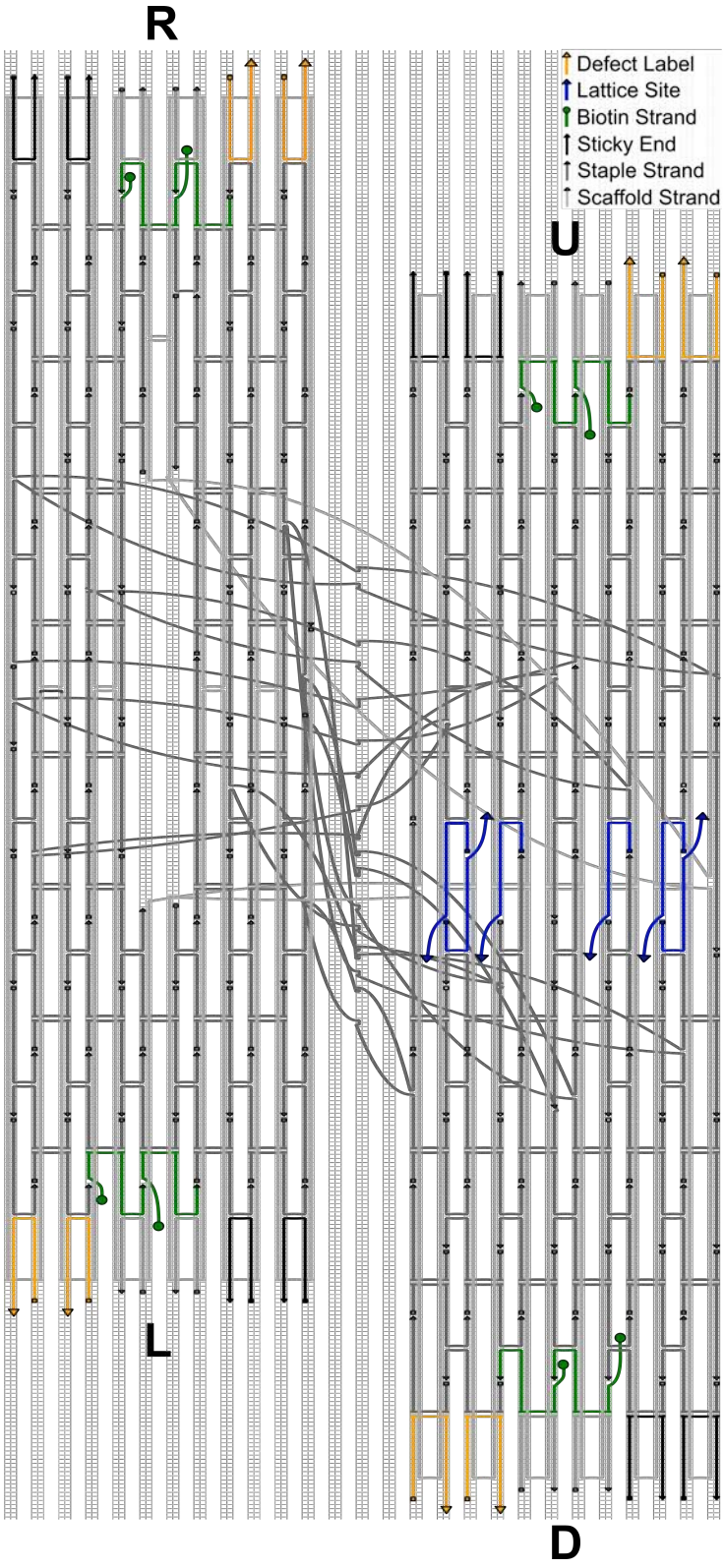

Figure S1 | Strand diagram for cross-shaped DNA origami A-tile. Strand diagram exported from caDNAno and altered to depict modifications to the tile for Xtal-PAINT imaging and tile array formation. Individual strand sequences and imager strand sequences can be found in **Tables S6-8**. Original design and naming convention for individual strands were adopted from Liu et al.

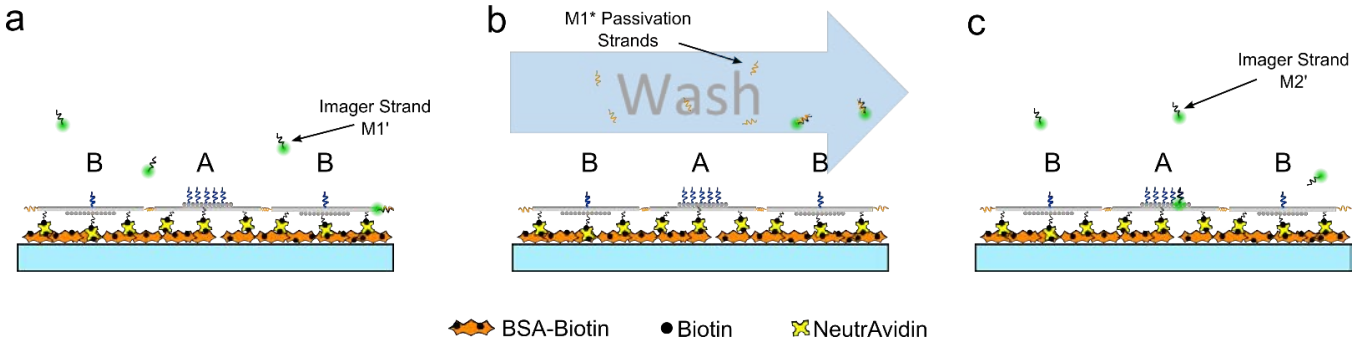

Figure S2 | Schematic depicting step-wise Xtal-PAINT imaging. (**a**) Schematic depicting defect label imaging of tile arrays bound to glass coverslip by biotin-avidin binding, with 3 nM imager strand M1' in solution. Biotinylated bovine serum albumin (BSA-Biotin) was used to functionalize the surface and immobilize tile structures by protein binding. (**b**) Rinse to remove imager strand M1' and deactivate remaining strands with 10 nM M1* imager passivation strands. Imager passivation strands were observed to effectively deactivate imager strands even when added directly to the imaging solution. (**c**) Lattice site imaging with 3 nM imager strand M2'. All buffer solutions contain 0.5x TBE 18mM $MgCl_2$, and 15,000 frames were captured at 6.66 Hz during each imaging step.

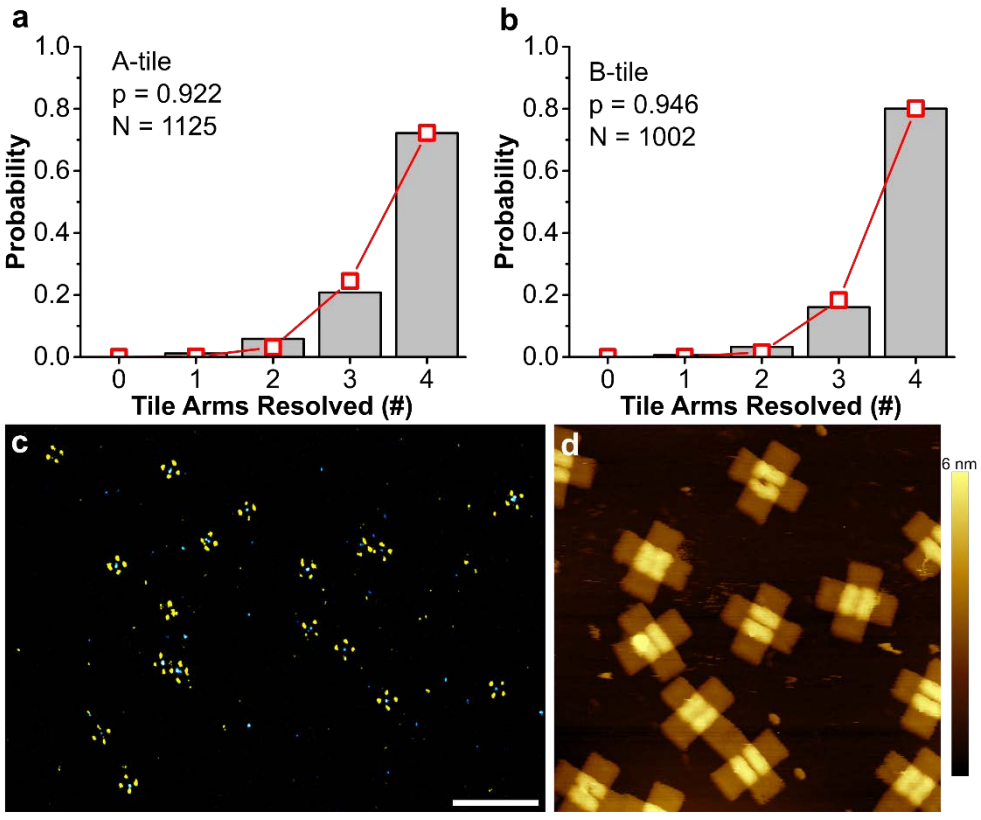

Figure S3 | Xtal-PAINT and AFM images of individual tiles. (**a**,**b**) For A-tiles and B-tiles imaged by Xtal-PAINT, probability histograms for the number of defect label sites counted per tile are shown (grey bars), where p is the probability of resolving defect label sites on an individual tile arm, and N is the total number of tiles counted. Binomial distributions (red) were generated from the results of counting to calculate p given that each tile has four arms. The data for individual tile counting statistics can be found in **Table S2**. (**c**) Xtal-PAINT image of individual B-tiles displaying defect labels (yellow) and lattice sites (blue). Mean localization precision for defect label and lattice images were 6.0 ± 4.0 nm and 11.3 ± 6.9 nm, respectively. Scale bar, 500 nm. (**d**) AFM image of individual B-tiles on mica, imaged in fluid (0.5x TBE with 12 mM $MgCl_2$ and 2mM $NiCl_2$). Image dimensions, 500 nm x 500 nm. To reduce homogeneous interactions between tiles, tile solutions were heated to 30 °C prior to deposition in fluid wells and on mica.

Table S2 | Individual tile counting statistics

	Count (A-tile)	Count (B-tile)	Probability (A-tile)	Probability (B-tile)	Binomial PDF (A-tile)	Binomial PDF (B-tile)
Number of Arms Resolved	**#arrays**	**#arrays**	**-**	**-**	**-**	**-**
4	812	802	0.722	0.800	0.723	0.801
3	234	161	0.208	0.161	0.245	0.183
2	66	33	0.059	0.033	0.031	0.016
1	13	6	0.012	0.006	0.002	0.001
***0**	0	0	0.000	0.000	0.000	0.000

* Tiles with no arms resolved could not be reliably distinguished in super-resolution images and were not counted

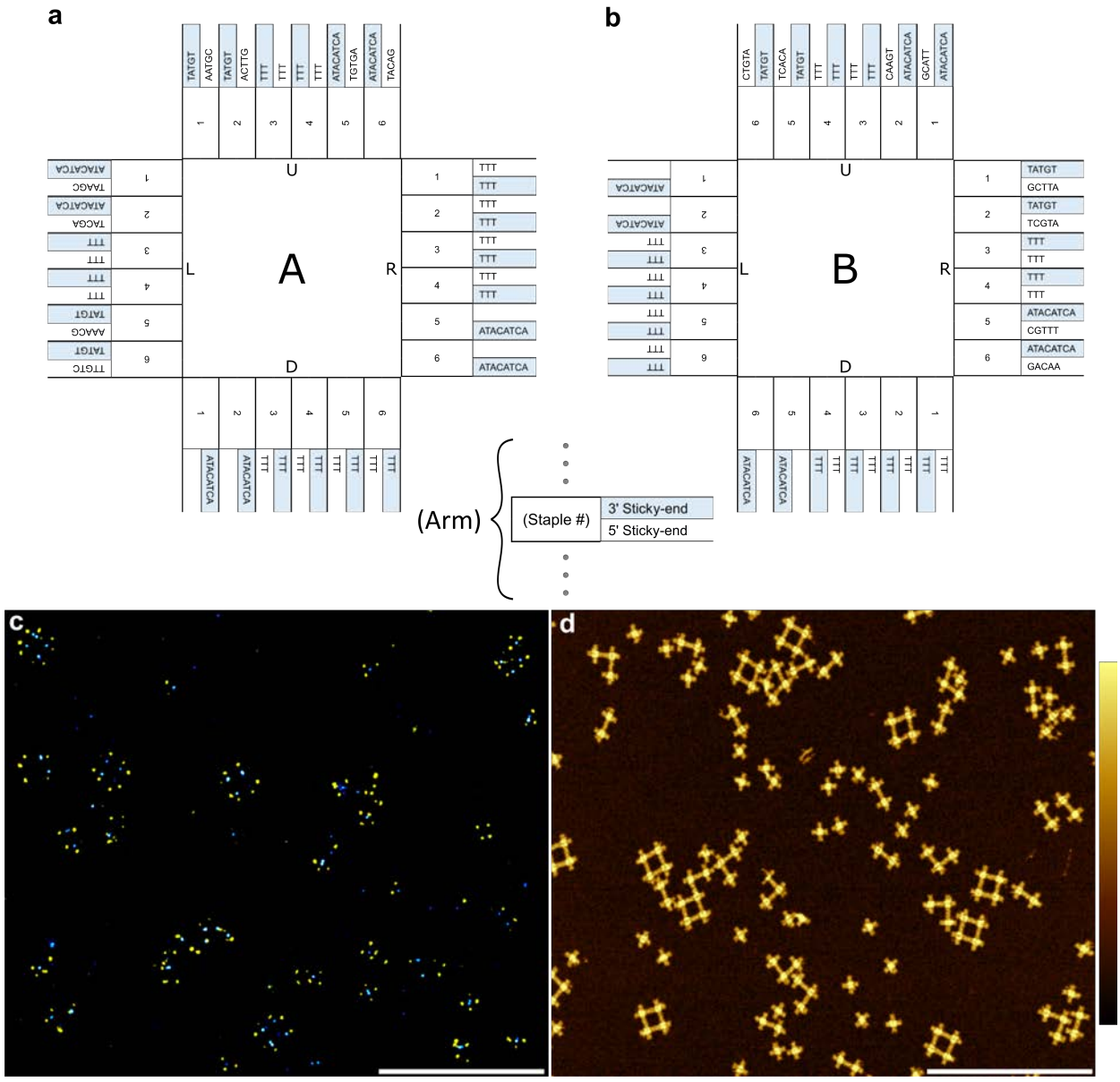

Figure S4 | Self-limiting 2x2-tile array design and Xtal-PAINT images. (**a**) and (**b**) Schematics of A-tile and B-tile, respectively, for self-limiting 2x2-tile arrays. Sticky-ends from two arms of each tile were replaced with 3 nt poly-Thymine extensions to deactivate the arms for sticky-end hybridization. Defect label strands on the passivated arms were replaced with modified defect label strands that lack 5' sticky-ends. (**c**) Xtal-PAINT image of 2x2-tile arrays annealed at 35 °C, displaying defect labels (yellow) and lattice sites (blue)**.** Individual tiles, 2-tile, 3-tile, and 2x2-tile arrays were resolved in the image. (**d**) AFM image of 2x2-tile arrays annealed at 35 °C and deposited onto mica. Mean localization precision for defect label and lattice images were 5.3 ± 3.6 nm and 8.4 ± 5.5 nm, respectively. Scale bars, 1 μm.

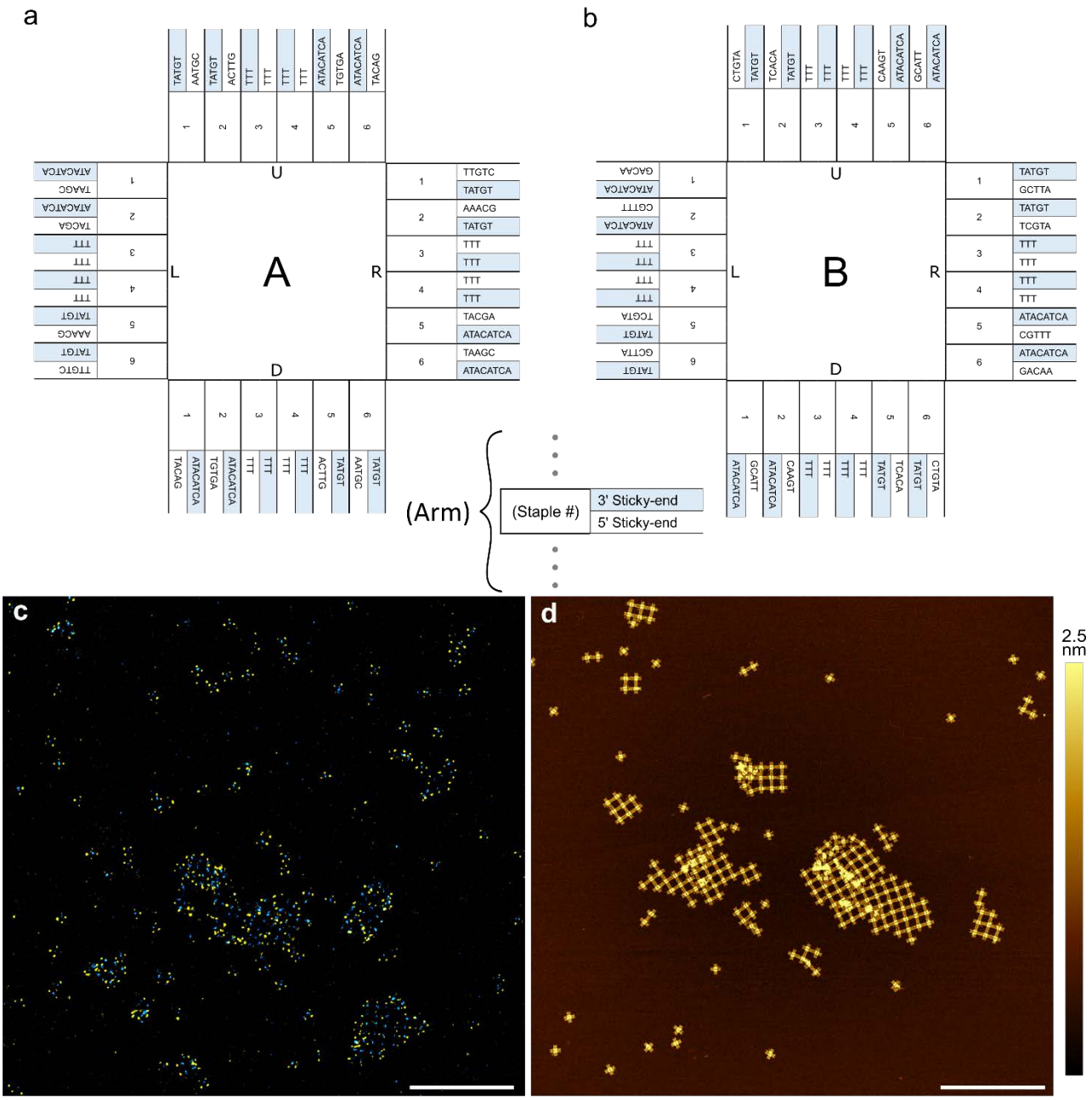

Figure S5 | Xtal-PAINT and AFM images of unconstrained tile arrays. (**a**) and (**b**) Schematics of A-tile and B-tile, respectively, for unconstrained tile arrays. Defect labels and sticky-ends reside on the outermost helices of each tile arm, and the central helices of each arm were passivated to blunt-end stacking interaction by 3 nt poly-Thymine extensions. (**c**) and (**d**) Xtal-PAINT and AFM image of unconstrained tile arrays on a coverslip and on mica, respectively. In the Xtal-PAINT image, large tile structures were observed that appear to consist of several overlapping tile arrays, consistent with structures observed in AFM images of tile arrays on mica. Mean localization precision for defect label and lattice images were 6.1 ± 4.1 nm and 9.0 ± 5.6 nm, respectively. Scale bars, 1 μm.

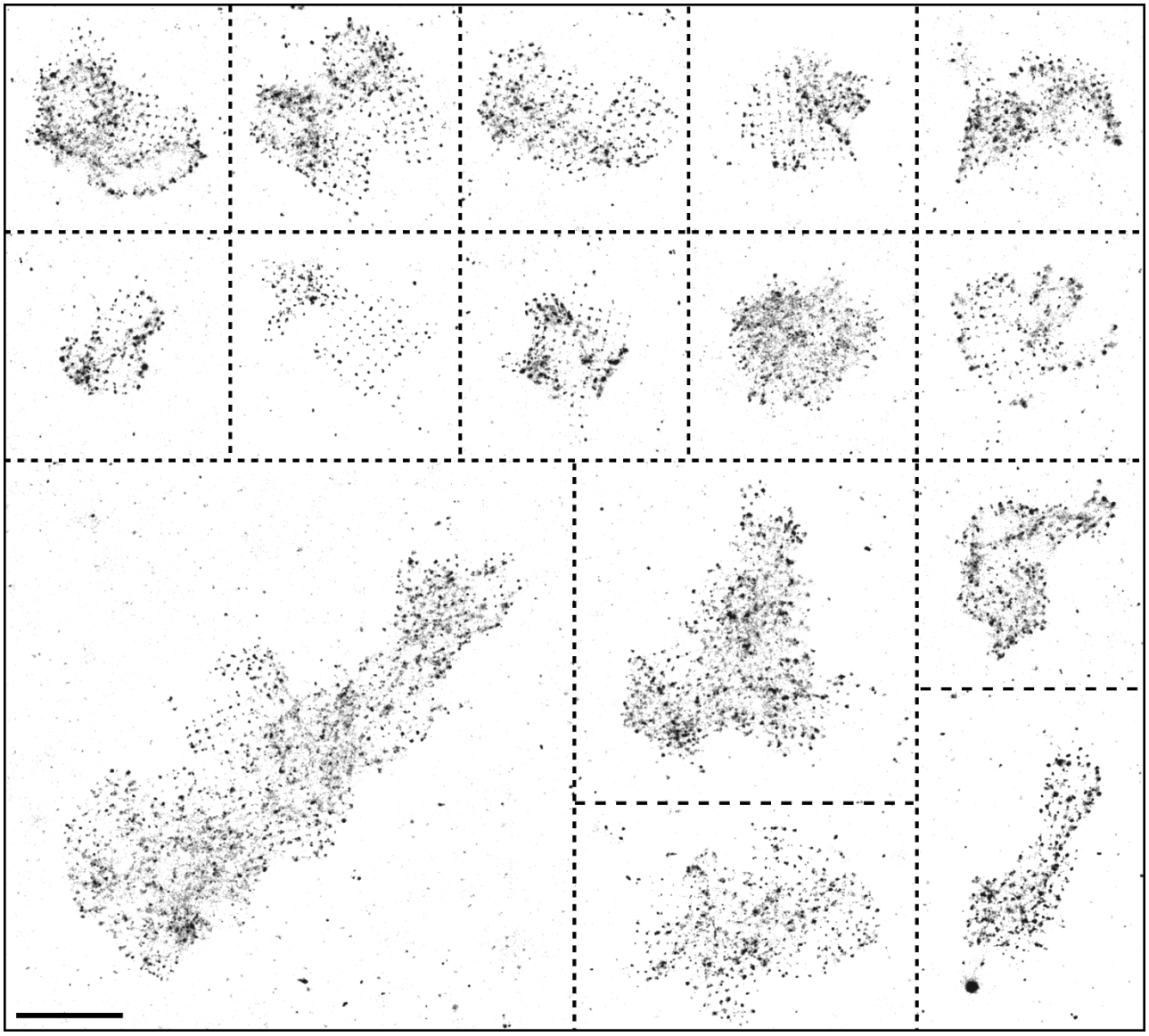

Figure S6 | Xtal-PAINT lattice images of large tile arrays with curvature. Inverted grayscale Xtal-PAINT lattice images of large tile arrays that were unable to flatten on the surface, indicated by indistinct, blurred regions of the array and/or curved lattice site paths. Blurring was observed in all the arrays due to poorly localized binding events, likely resulting from imager strand binding to lattice sites located outside of the focal plane and/or overlapping binding events. These effects were rarely observed in tile arrays smaller than 1 μm x 1 μm, though it is unlikely that the curvature observed in large arrays was caused by global curvature since no tube-like structures were observed. Rather, tile arrays were unable to relax or flatten on the surface due to immobilization by biotin-avidin binding. Large tile arrays are more likely to experience large fluctuations away from planarity due to local fluctuations of the solution, and any deformation that occurs in tile arrays while binding to the surface may be trapped in the structure. Scale bar, 1 μm.

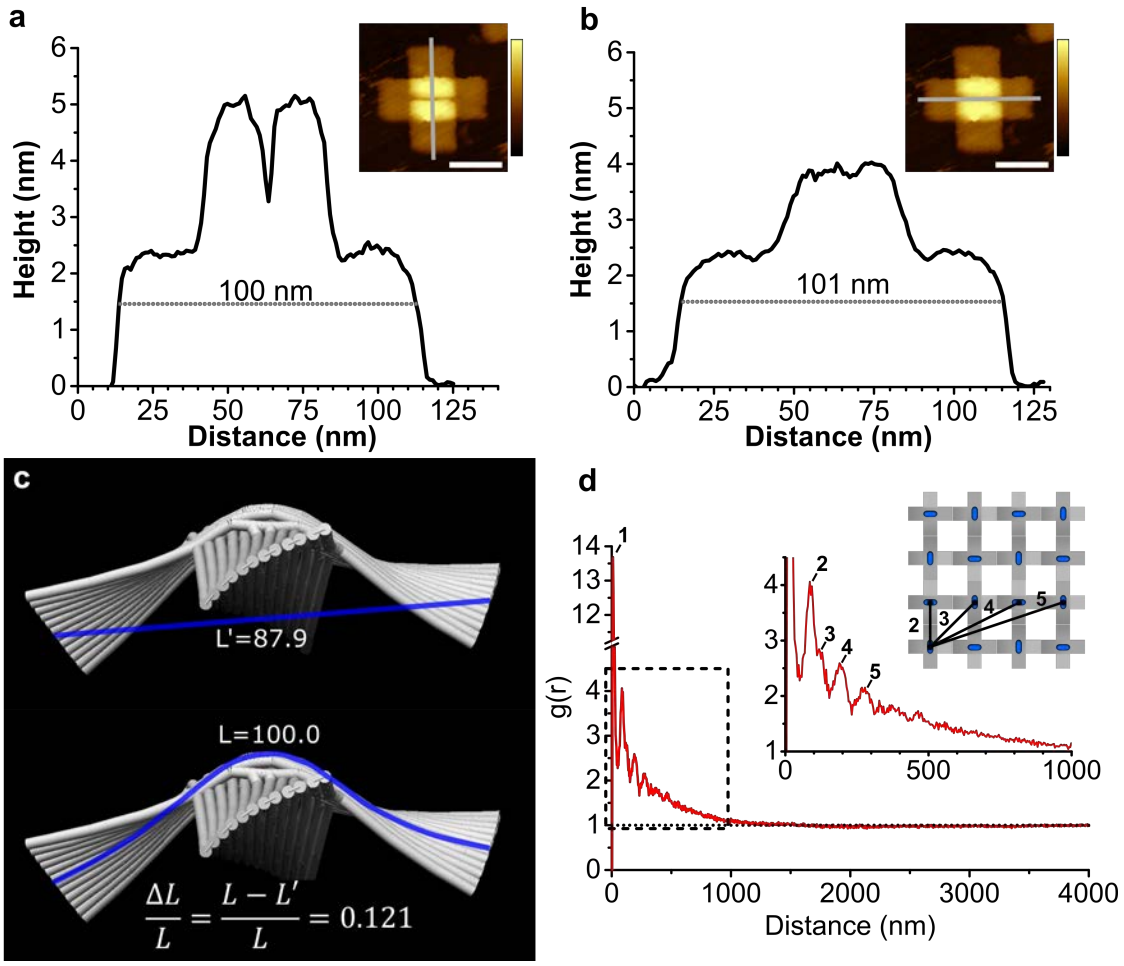

Figure S7 | Analysis of cross-shaped DNA origami tile dimensions. (**a**) and (**b**) Topographic profiles of a cross-shaped DNA origami tile in the directions perpendicular to and parallel to the central indent of the tile, respectively. The dimensions of the tile along both directions are approximately 100 nm, in agreement with the dimensions reported by Liu et. al. Scale bars, 50 nm. AFM height color bar, 5.5 nm. (**c**) Cando-generated model of the cross-shaped DNA origami tile. The contraction in the dimensions of the Cando model due to curvature and twist were calculated by the difference between the path length of the helices and the straight line distance between each end of a tile arm. The observed contraction in the length of the tile arm was approximately 12%. (**d**) Radial distribution function of an Xtal-PAINT lattice image of unconstrained tile arrays. The first peak was observed at 10 nm (peak 1). The peak corresponding to the center to center distance between bound tiles in a tile array was observed at 87.4 nm (peak 2), a ~13% contraction in the dimensions of the tile relative to the tile dimensions observed in AFM images of tiles on mica in **a,b**. This result is in agreement with the contraction observed in the Cando tile model. Additional peaks were observed at 123 nm, 195 nm, and 275 nm (peaks 3-5), corresponding to the 2nd, 4th, and 7th nearest neighbor distances for a square lattice with a lattice constant of 87 nm. Peak positions were determined by fitting individual peaks with Gaussian functions. Statistics for the results of peak fitting for peaks 2-5 are provided in **Table S3**.

Table S3 | Peak fitting statistics for unconfined tile arrays

	Peak position		Peak width		sigma	FWHM	Height	Statistics	
	Value (nm)	Standard Error	Value (nm)	Standard Error	Value (nm)	Value (nm)	Value	Reduced Chi-Sqr	Adj. R-Square
Peak 2	87.40071	0.51087	26.5205	5.14706	13.26025	31.2255	1.63016	0.01118	0.94422
Peak 3	122.7505	7.59605	20.76644	18.22743	10.38322	24.45061	0.46998	0.15444	0.94465
Peak 4	194.92566	6.28781	30.5346	18.75183	15.2673	35.95175	0.65668		
Peak 5	275.39338	11.32762	37.26473	32.74182	18.63236	43.87586	0.43181		

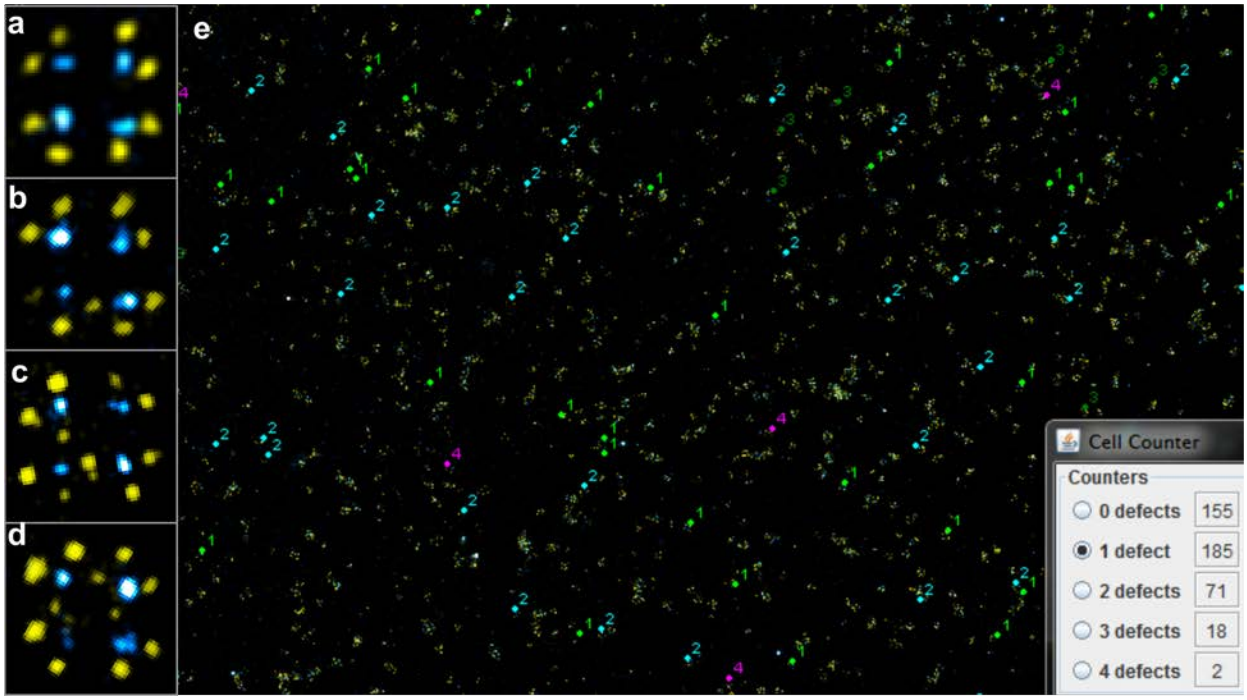

Figure S8 | Defect counting method for 2x2-tile arrays. (**a-d**) Examples of 2x2-tile arrays imaged by Xtal-PAINT with 0, 1, 2, and 3 defects, respectively. For self-limiting 2x2-tile array samples annealed at 25, 30, and 35 °C, 2x2-tile arrays were counted by the number of defects resolved at bound arms. The data for 2x2-tile array defect counting can be found in **Table S4**. (**e**) Example of counting window for 2x2-tile array defect counting. Counting results for sample annealed at 25 °C are shown.

Table S4 | Self-limiting 2x2-tile array defect counting statistics

	Count (25°C)	Count (30°C)	Count (35°C)	Probability (25°C)	Probability (30°C)	Probability (35°C)	Binomial PDF (25°C)	Binomial PDF (30°C)	Binomial PDF (35°C)
Number of Defects	**#arrays**	**#arrays**	**#arrays**	**-**	**-**	**-**	**-**	**-**	**-**
0	155	146	231	0.360	0.482	0.606	0.359	0.481	0.605
1	185	132	127	0.429	0.436	0.333	0.419	0.386	0.324
2	71	23	21	0.165	0.076	0.055	0.184	0.116	0.065
3	18	2	2	0.042	0.007	0.005	0.036	0.016	0.006
4	2	0	0	0.005	0.000	0.000	0.003	0.001	0.000

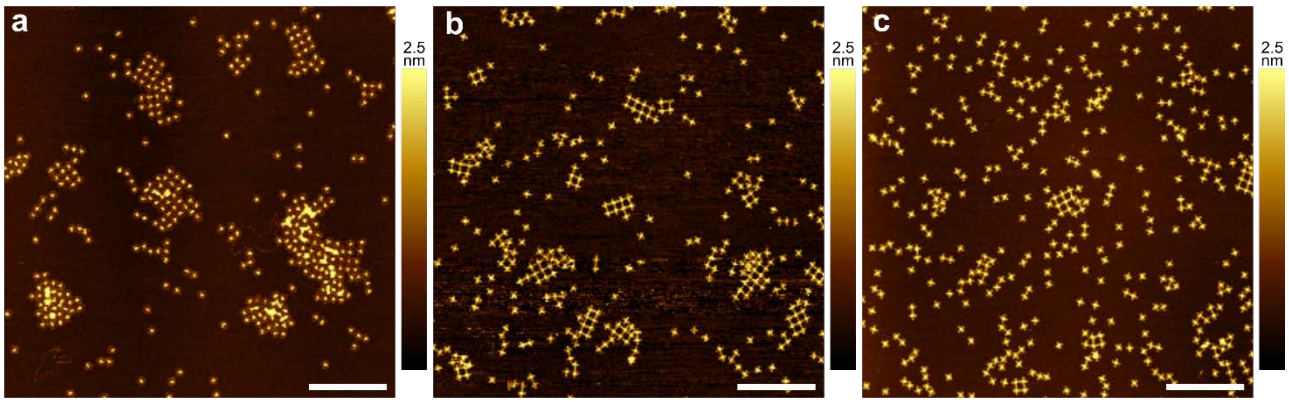

Figure S9 | AFM images of tile arrays formed by constant temperature annealing. (**a-c**) AFM images of unconstrained tile arrays on mica, annealed for three hours at 35, 37, and 40 °C, respectively, in 0.5x TBE 8mM $MgCl_2$. As expected, the average size of tile arrays was observed to decrease with anneal temperature, and the few arrays observed in the sample annealed at 40 °C likely formed during deposition onto mica. All samples were prepared in parallel and immediately deposited on mica after annealing, though cooling of each solution on contact with mica likely contributed to a small degree of array formation in each case. These results indicate that the temperature of formation of tile arrays by sticky-end hybridization in TBE/Mg^{2+} buffer (0.5x TBE 8 mM $MgCl_2$) is below 40 °C. Scale bars, 1 μm.

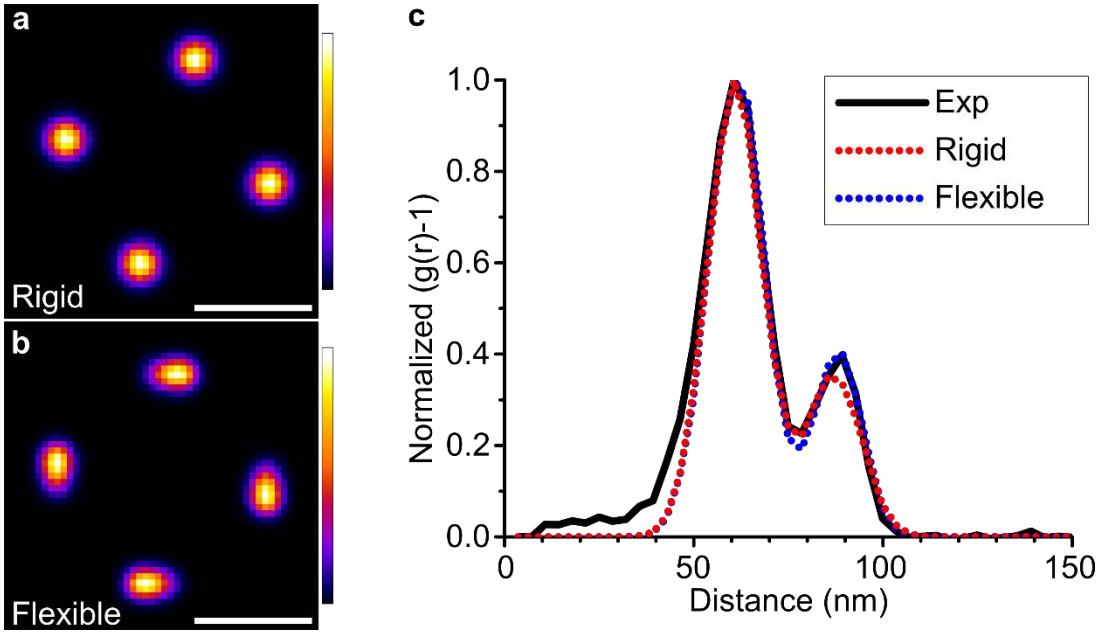

Figure S10 | Simulated radial distribution function of rigid and flexible tile models. (**a**) Probability distribution of tile defect label positions for a rigid tile model, generated by Monte Carlo methods ($N=10^5$). For a rigid model, each point distribution is rotationally symmetric. (**b**) Probability distribution of tile defect label positions for a "flexible" tile model with an additional degree of freedom to account for twisting, generated by Monte Carlo methods ($N=10^5$). In comparison to the rigid model, the point distributions of the flexible tile model are elongated tangent to the tile. Scale bars, 50 nm. Probability color bar, linear from 0 to 1 AU. (**c**) Radial distribution functions of the rigid and flexible tile models plotted with the experimental g(r) for comparison. For a valid comparison of the shape of each distribution, the contribution of random tile positions was removed from the experimental distribution by subtracting 1 and all distributions were normalized by the maximum values of each distribution (corrections validated in Figure S12). The shape, position, and relative height of the second peak of the experimental distribution could not be accounted for with a rigid tile model, demonstrating the need for a tile model that accounted for the effect of arm twist on the positions of defect labels.

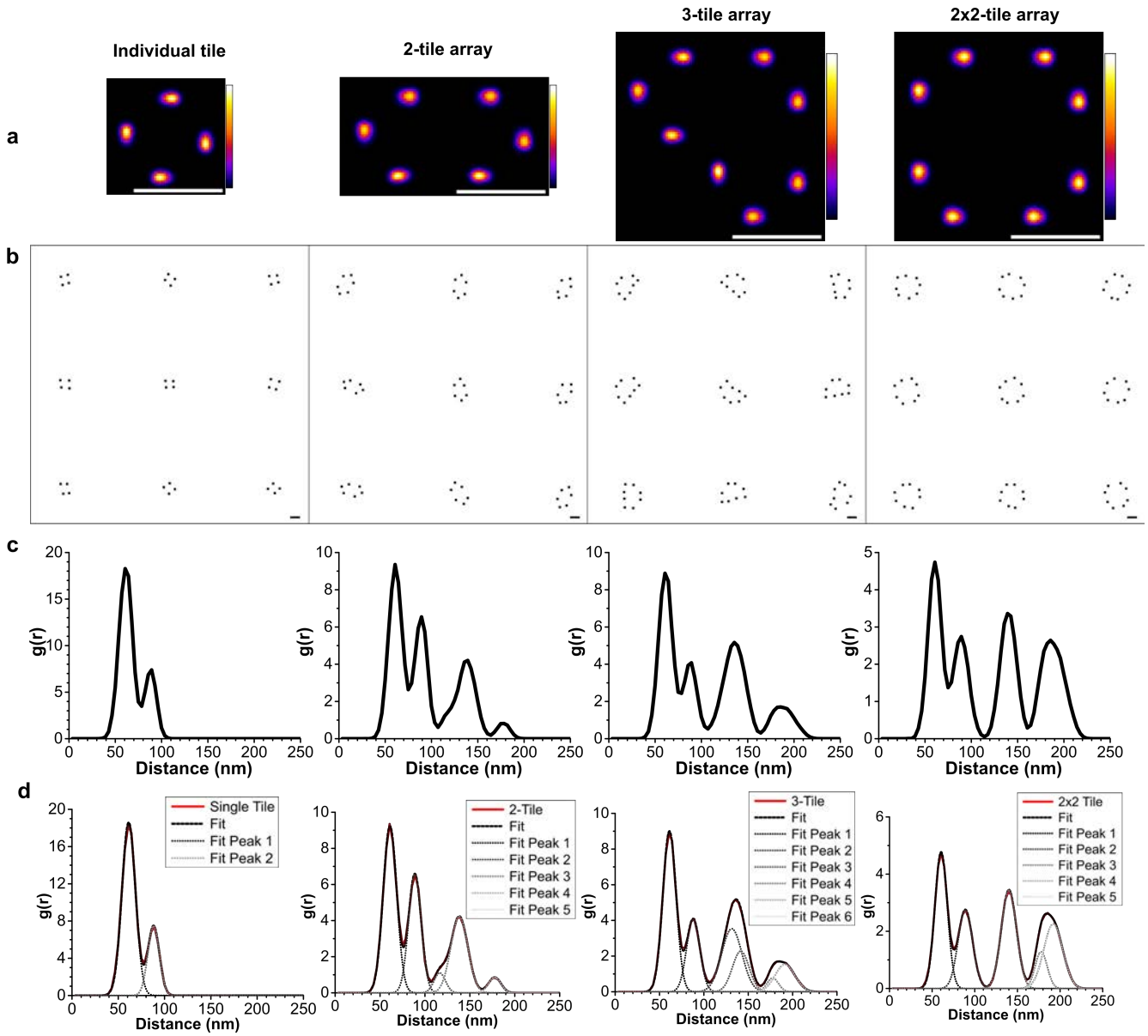

Figure S11 | Simulated radial distribution functions for tile arrays. (**a**) Probability distributions of defect label positions for the flexible models of individual tiles, 2-tile arrays, 3-tile arrays, and 2x2-tile arrays. Scale bars, 100 nm. (**b**) Simulated images of tile structures with uniform spacing, random orientation, and random defect label positions defined by the corresponding probability distributions in **a**. The densities of tiles and arrays were equivalent for all images. (**c**) Radial distribution functions of simulated tiles and arrays corresponding to **a** and **b**. For each structure, g(r) was calculated from a stack of 16 images, each image containing 625 evenly spaced structures, a total of 10^4 simulated structures. (**d**) Peak fitting of g(r) for the simulated distributions. Each distribution was approximated as a sum of Gaussian distributions, and the results of fitting were used for linear decomposition of experimental spectra.

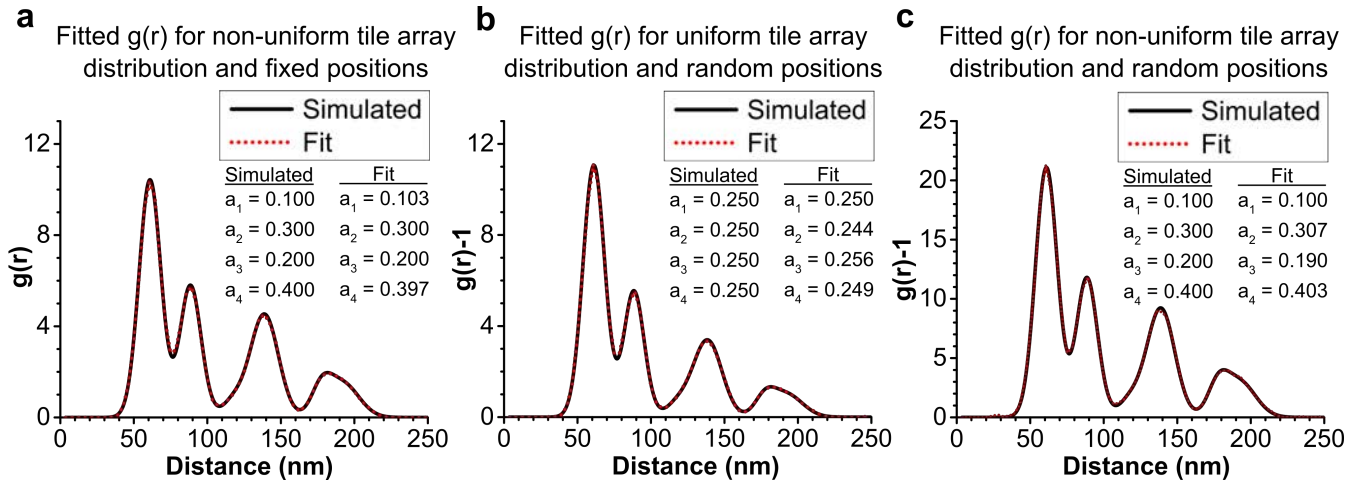

Figure S12 | Radial distribution function for randomized position and tile distribution. (**a**) Simulated g(r) for a sample with a non-uniform but known distribution of tiles and arrays. To determine if the distribution of tile arrays in an Xtal-PAINT image could be quantified from g(r), the simulated g(r) was fitted with a linear combination of the individual tile, 2-tile array, 3-tile array, and 4-tile array spectra. The fitted g(r) is plotted along with the simulated g(r). The distribution of tiles and arrays was accurately predicted by the fraction of each component in the fitted g(r), validating the use of g(r) to quantify distributions of tile arrays. (**b**) Simulated g(r) and fitted spectra for a uniform distribution of tile arrays with randomized positions within the image. (**c**) Simulated g(r) and fitted spectra for a non-uniform distribution of tile arrays with randomized positions within the image. The spectra used for fitting did not have randomized positions (**Figure S11**), though at low point densities the contribution of randomness can be effectively removed by subtracting 1 from g(r). This is demonstrated by the fitted spectra in **b** and **c**.

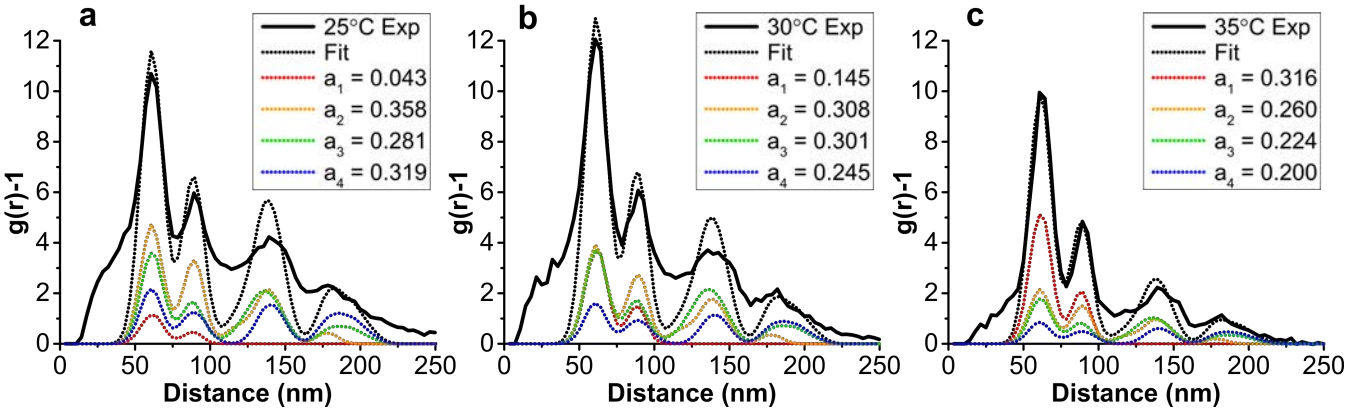

Figure S13 | Linear decomposition of experimental g(r) into simulated spectra. (**a-c**) Experimental, fitted, and component g(r) for constrained 2x2-tile array samples annealed at 25, 30, and 35 °C, respectively. The fitted g(r) were generated by spectral decomposition of the experimental g(r) into a linear combination of spec single tile (X_1), 2-tile array (X_2), 3-tile array (X_3), and 2x2-tile array (X_4) spectra. Fit = $a_1X_1 + a_2X_2 + a_3X_3 + a_4X_4$, where a_1-a_4 represent the fraction of tiles in each size of tile array out of the total number of tiles. The isolated component spectra are shown in **Figure S11**. The fraction of tiles bound by sticky-end hybridization (a_2-a_4) was observed to decrease with anneal temperature. The deviation of fitted g(r) from experimental g(r) also decreased with anneal temperature due to a decrease in the fraction of tile structures that are not accounted for by the isolated component spectra (**Figure S14**).

Table S5 | Statistics for fitting of experimental g(r)

	a1		a2		a3		a4		Statistics	
	Value	Standard Error	Value	Standard Error	Value	Standard Error	Value	Standard Error	Reduced Chi-Sqr	Adj. R-Square
25 °C	0.04254	0.06067	0.35795	0.19343	0.28067	0.22905	0.31885	0.17504	2.09289	0.61456
30 °C	0.14535	0.06201	0.30843	0.19088	0.30118	0.22692	0.24504	0.17802	1.89167	0.72172
35 °C	0.31642	0.04411	0.25982	0.1232	0.22424	0.14351	0.19952	0.11692	0.32711	0.92639

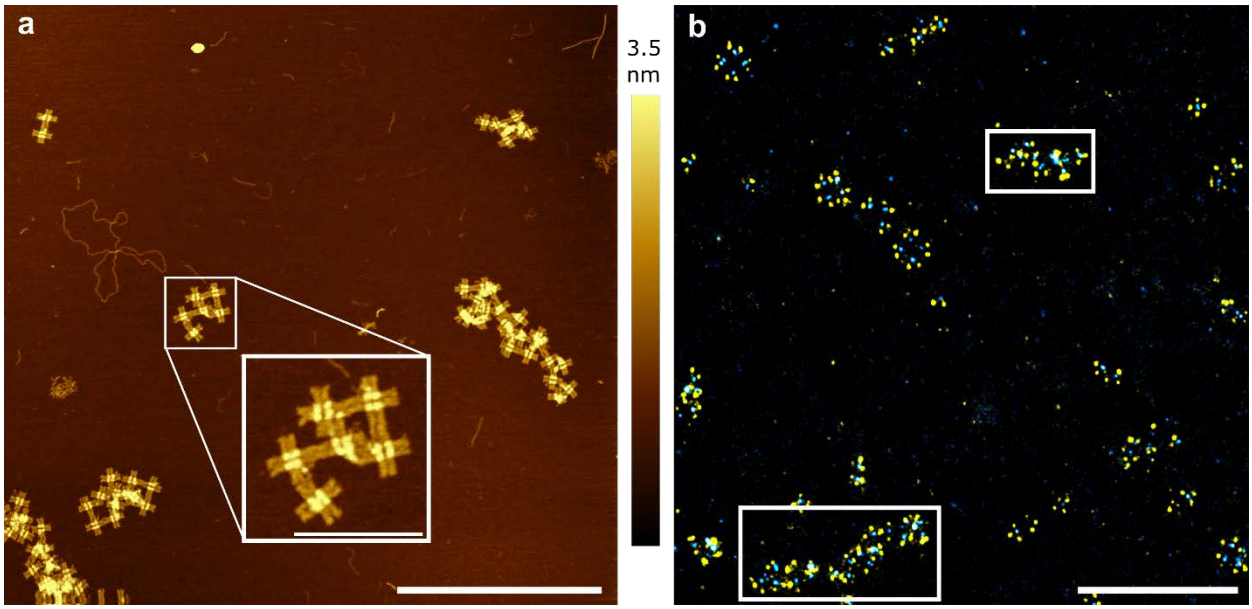

Figure S14 | Xtal-PAINT and AFM images of extended 2x2-tile arrays. (**a**) AFM image of a self-limiting 2x2-tile array sample on mica. In the image, several tile arrays were observed that failed to terminate at 2x2-tile arrays. The tile array magnified in the image demonstrates out-of-plane sticky-end hybridization, which enables tile arrays to extend beyond the intended 2x2-tile structure. Several larger tile arrays were also observed in the image. (**b**) Xtal-PAINT image of a self-limiting 2x2-tile array sample. Several large tile structures were resolved that failed to terminate at 2x2-tile arrays due to out-of-plane sticky-end hybridization, closely resembling tile arrays observed in **a**. Mean localization precision for defect label and lattice images were 5.8 ± 3.9 nm and 7.9 ± 5.3 nm, respectively. Scale bars, 1 μm. Inset scale bar, 250 nm.

Table S6 | Strand sequences for cross-shaped DNA origami tile (body strands)

Name	Sequence	Length (bp)	Type
CO-M-001	AGCTAATGCAGAACGCGCCTGTTTTAATATCC	32	
CO-M-002	CATCCTAATTTGAAGCCTTAAATCTTTTATCC	32	
CO-M-003 [B]	\5Biosg\ TTTTTTTTTT TGAATCTTGAGAGATAACCCACAAAACAATGA	42	Biotin-labeled
CO-M-004 [B]	\5Biosg\ TTTTT AATAGCAATAGATGGGCGCATCGTACAGTATC	37	Biotin-labeled
CO-M-005	GGCCTCAGCTTGCATGCCTGCAGGGAATTCGT	32	
CO-M-006	AATCATGGTGGTTTTTCTTTTCACCCGCCTGG	32	
CO-M-007	CCCTGAGAGAGTTGCAGCAAGCGGGTATTGGG	32	
CO-M-008	CGCCAGGGTCATAGCTGTTTCCTGGACGGCCA	32	
CO-M-009 [c]	GTGCCAAGGAAGATCGCACTCCAGATAGGTCA	32	
CO-M-010	CGTTGGTGTAGCTATCTTACCGAATTGAGCGC	32	
CO-M-011 [c]	TAATATCAACCAACGCTAACGAGCCCGACTTG	32	
CO-M-012	CGGGAGGTTTTACGAGCATGTAGAACATGTTC	32	
CO-M-013	CTGTCCAGACGACGACAATAAACAAACCAATC	32	
CO-M-014	AATAATCGCGTTTTAGCGAACCTCGTCTTTCC	32	
CO-M-015	AGAGCCTACAAAGTCAGAGGGTAAGCCCTTTT	32	
CO-M-016	TAAGAAAAGATTGACCGTAATGGGCCAGCTTT	32	
CO-M-017	CCGGCACCCACGACGTTGTAAAACTGTGAAAT	32	
CO-M-018	TGTTATCCGGGAGAGGCGGTTTGCTCCACGCT	32	
CO-M-019	GGTTTGCCCCAGCAGGCGAAAATCAATCGGCC	32	
CO-M-020	AACGCGCGGCTCACAATTCCACACCCAGGGTT	32	
CO-M-021	TTCCCAGTGCTTCTGGTGCCGGAAGTGGGAAC	32	
CO-M-022	AAACGGCGGTAAGCAGATAGCCGAAACTGAAC	32	
CO-M-023	ACCCTGAAATTTGCCAGTTACAAATTCTAAGA	32	
CO-M-024	ACGCGAGGGCTGTCTTTCCTTATCAAGTAATT	32	
CO-M-025	AATATAAAGTACCGACAAAAGGTAATTCCAAG	32	
CO-M-026	AACGGGTAGAAGGCTTATCCGGTAATAAACAG	32	
CO-M-027	CCATATTAATTAGACGGGAGAATTACAAAGTTACC	35	
CO-M-028	GTCGGATTCTCCACCAGGCA	20	
CO-M-029	AAGCGCCAATTAAGTTGGGTAACGAACATACG	32	
CO-M-030	AGCCGGAAGCCAGCTGCATTAATGCTGTTTGATGGTGTCTTCCTGTAG	48	
CO-M-031	CCTGTCGTGCATAAAGTGTAAAGCGATGTGCT	32	
CO-M-032	GCAAGGCGTTCGCCATTCAGGCTGCGCAACTG	32	
CO-M-033	GGAAGCGCTTTATCCCAATCCAAAAAGCAAAT	32	
CO-M-034	CAGATATATTAAACCATACGGAAATTACCCAAAAGAACTGGCATGATTA	49	
CO-M-035	AGGCATTTTCGAGCCAGTACTCATCG	26	
CO-M-036	AGAACAAGTACCGCGCCCAATAGCTAAGAAAC	32	
CO-M-037	GATTTTTTACAGAGAGAATAACATAAAAACAG	32	
CO-M-038	TTGGGAAGCAGCTGGCTTAAAGCTAGCTATTTTTGAGAGATCTGGAGCA	49	
CO-M-039	CCTAATGAACTGCCCGCTTTCCAGCCCTTATA	32	
CO-M-040	AATCAAAAGAATAGCCCTTTAAATATGCATTCTACTAATAGTAGTAACATTAT	53	
CO-M-041	GAGATAGGGTTGTCAGGATTAG	22	
CO-M-042	TTGCGCTCGTGAGCTAACTCACATGATAGCCC	32	
CO-M-043	TATTACGCGGCGATCGGTGCGGGCGAGGATTT	32	
CO-M-044	CAGCCTTTGTTTAACGTCAAAAATTTTCAATT	32	
CO-M-045	GGAATCATCAAGCCGTTTTTATTTGTTATATA	32	
CO-M-046 [c]	CCAACATGTTGTGCCCGTATA	21	
CO-M-047	ACTATATGCTCCGGCTTAGGTTGGTCATCGTA	32	
CO-M-048	ACCTGAGCAGAGGCGAATTATTCAGAAAATAG	32	

CO-M-049	AGAAGTATAATAGATAATACATTTCTCTTCGC	32	
CO-M-050	TAAAACATCTTTAATGCGCGAACTTAATTGCG	32	
CO-M-051	CTATTAGTCGCCATTAAAAATACCATAGATTA	32	
CO-M-052	GAGCCGTCTAGACTTTACAAACAATTCGACAA	32	
CO-M-053	AATCGCGCAAAAGAAGTTAGTTAGCTTAAACAGCTTGATACGCCCACGC	49	
CO-M-054	TTTTTAACTAAATGCTGATGCAAAATTGAGAA	32	
CO-M-055	TCGCCATATTTAACAACGTTGCGGGGTTTTAAGCCCAATAGGAACCTTGTCGTC	54	
CO-M-056	CAAGACAAAAATCATAGGTCTGAGACAAACAT	32	
CO-M-057	CAAGAAAAATTGCTTTGAATACCAAGTTACAA	32	
CO-M-058	CTCGTATTGGTGCACTAACAACTAGAACGAAC	32	
CO-M-059	CACCAGCAGGCACAGATTTAATTTCTCAATCATAAGGGAACCGAACTGA	49	
CO-M-060	TGCTGGTAATATCCAGAACAATATAAGCGTAA	32	
CO-M-061	GAATACGTGAAGATAAAACAGAGGATCTAAAA	32	
CO-M-062	TATCTTTAAAATCCTTTGCCCGAACCGCGACCTGC	35	
CO-M-063	CGAAACAAAGTAATAACGGA	20	
CO-M-064	TTCGCCTGCAAAATTAATTACATTAATAGTGA	32	
CO-M-065	ATTTATCAAGAACGCGAGAAAACTAGTATAAAGCCAATAAAGAATACAC	49	
CO-M-066	ATATGCGTTATACAAATTCTTACCTTTTCAAA	32	
CO-M-067	TATATTTTGACGCTGAGAAGAGTCTAACAATT	32	
CO-M-068	TGATTTGATACATCGGGAGAAACACAACGGAG	32	
CO-M-069	TTTGGATTATACCTGATAAATTGTGTCGAAATCGTTATTA	40	
CO-M-070	ATTTTAAAGGAATTGAGGAAGGTTTGAGGCGG	32	
CO-M-071	TCAGTATTAACCCTTCTGACCTGATACCGCCA	32	
CO-M-072	GCCATTGCAACAGGAAAAACGCTCTGGCCAAC	32	
CO-M-073 [c]	AGAGATAGAACACCGCCTGCAACAAAATCAAC	32	
CO-M-074	AGTAGAAAAGTTTGAGTAACATTA	24	
CO-M-075	ATTTGTATCATCGCTTCTGAATTACAGTAACA	32	
CO-M-076	GTACCTTTATTACCTTTTTTAATGCGATAGCT	32	
CO-M-077 [c]	TAGATTAAAGTTAATTTCATCTTCTTAGTATC	32	
CO-M-078	TCATAATTACTAGAAAAAGCCTGTTGACCTAA	32	
CO-M-079	ATTTAATGATCCTTGAAAACATAGGAAACAGT	32	
CO-M-080	ACATAAATACGTCAGATGAATATATGGAAGGA	32	
CO-M-081 [c]	TTAGAACCAATATAATCCTGATTGTCATTTTG	32	
CO-M-082	CGGAACAATATCTGGTCAGTTGGCGTGCCACG	32	
CO-M-083	CTGAGAGCAATAAAAGGGACATTCATGGAAAT	32	
CO-M-084 [c]	ACCTACATTTTGACGCTCAATCGTCAGTCACA	32	
CO-M-085	CGACCAGTCAGCAGCAAATGAAAATCAAACCC	32	
CO-M-086 [B]	\5Biosg\ TTTTTTTTTT TCAATCAAAGAAACCACCAGAAGGATGATGGC	42	Biotin-labeled
CO-M-087 [B]	\5Biosg\ TTTTT AATTCATCTACCATATCAAAATTATAGATTTT	37	Biotin-labeled
CO-M-088	CAGGTTTACAATATATGTGAGTGATTAATTTT	32	
CO-M-089	CCCTTAGAGTTTGAAATACCGACCCACCGGAA	32	
CO-M-090	ATAAGCAAAAATTCGCGTTAAATTTTTGTTAA	32	
CO-M-091	CTCATATAAAAGATTCAAAAGGGTAAGATTGT	32	
CO-M-092 [B]	\5Biosg\ TTTTT CGAACGAGAAATGGTCAATAACCTTTAGAACC	37	Biotin-labeled
CO-M-093 [B]	\5Biosg\ TTTTTTTTTT ATAGTCAGGGAAGCCCGAAAGACTCAATTCTG	42	Biotin-labeled
CO-M-094	ACCACATTTTACGAGGCATAGTAATGACTATT	32	
CO-M-095 [c]	CAAGAGTAATCAACGTAACAAAGCTTAGGAAT	32	
CO-M-096 [c]	CAGTGAATGCGCATAGGCTGGCTGACCTTCAT	32	
CO-M-097 [c]	CTATCATAATTCATCAGTTGAGATTGCTCATT	32	
CO-M-098	CGCGTTTTAATCAGGTCTTTACCCGAGCAACA	32	
CO-M-099	ATATTTTCTGTAACAGTTGATTCCTCAAATAT	32	
CO-M-100	CCGGAGACGCAAGGATAAAAATTTGTTTAGCT	32	

CO-M-101	ATCAGCTCAAGCCCCAAAAACAGGGAGAAAGG	32	
CO-M-102	AATCAGAAATTTTTTAACCAATAGGAACGCCA	32	
CO-M-103	ATTTCAACAGTCAAATCACCATCACGGTTGAT	32	
CO-M-104	TCATTCCAATTTGGGGCGCGAGCTAAGCCTTT	32	
CO-M-105	AAATCAAAAATTCGAGCTTCAAAGTGGAAGTT	32	
CO-M-106	GTAGAAAGACCCTCGTTTACCAGAATGACCAT	32	
CO-M-107 [c]	CAGACCAGAAGGCTTGCCCTGACGTATTACAG	32	
CO-M-108	CAGAACGAGAAAGAGGACAGATGAACGGTGTA	32	
CO-M-109 [c]	AAAACCAAACTAACGGAACAACATAGAAACAC	32	
CO-M-110 [c]	ACCGGAAGAGTTCAGAAAACGAGACGACGATA	32	
CO-M-111	GGCATCAAACTAAAGTACGGTGTCCGAACCAG	32	
CO-M-112	TTCAACCGAATACTTTTGCGGGAGGAAAAGGT	32	
CO-M-113	TCAAAAATTCAATCATATGTACCCATATGATA	32	
CO-M-114	CTAGCATGAATTCGCGTCTGGCTGTTCCGAAATCGGCAAAATTCGGGAAA	50	
CO-M-115	GACCCTGTTTCTAGCTGATAAATTTCGTAAAA	32	
CO-M-116	AACAGTTAACCAGAGCCGCCGCCAGAACCGCC	32	
CO-M-117	CTTTAAACCAAACTCCAACAGTTGAGTGTTGTTCGTAGAAGAACTCAAACTTTGAATGG	59	
CO-M-118	TAAAACGAAATAGCGAGAGGCTTTCTCAAATG	32	
CO-M-119	CCAACTTTGTAGTAAATTGGGCTTTACGTTAA	32	
CO-M-120	AAGTTTTGGTTGGGAAGAAAAATCGAGATGGTTCAATATTTATCGGCCT	49	
CO-M-121	AGAGTACCTATTCATTGAATCCCCTGCAAAAG	32	
CO-M-122 [c]	CATCCAATAATGCTGTAGCTCAACATGTTT	30	
CO-M-123	AGAGGGTAAATCGGTTGTACCAAAAGCATTAA	32	
CO-M-124	CCAGCTTTAATCGATGAACGGTAAAATGCCGG	32	
CO-M-125	AACAAGAGCATCAACATTAAATGTGAGCGAGTAACAACTTAAGGAAACCGAGGAAA	56	
CO-M-126	CTGAATCTAAATCATACAGGCAAGTCAGAGCATGAAAGGGGCTGGGGTG	49	
CO-M-127	GTCATAAATTTAATTGCTCCTTTTCTTAATTG	32	
CO-M-128	GTCAGGACCCAGAGGGGGTAATAGGCGGAATC	32	
CO-M-129	AACGAGGCGCAGACGGAACTTTAATCATTGTGTTATACCA	40	
CO-M-130 [D]	CTGGCTCAAATTACCTTATGCGATAATGACAATTACTTGTGA	42	M2' Dock
CO-M-131 [D]	CCAATACTTAAAATGTTTAGACTGGTAGCATTTTACTTGTGA	42	M2' Dock
CO-M-132 [ND]	GCTTAGAGGATAAGAGGTCATTTTTGAAACAT	32	
CO-M-133 [D]	ATAAAGCCGCAAAGAATTAGCAAACCACCACCTTACTTGTGA	42	M2' Dock
CO-M-134 [D]	CTGAGAGTCTACAAAGGCTATCAGACTTGAGCTTACTTGTGA	42	M2' Dock
CO-M-135 [D]	CATTTGGGATTATCACCGTCACCGGTCATTGCTTACTTGTGA	42	M2' Dock
CO-M-136 [ND]	CTCAGAGCACCGCCACCCTCAGAGATTAAGCA	32	
CO-M-137 [ND]	GAAAGTATTCGGAACCTATTATTCTGCGGATG	32	
CO-M-138 [ND]	CCACAGACACAAACTACAACGCCTGATAGCGT	32	
CO-M-139 [D]	CAACCATCCGATAGTTGCGCCGACTTTAAGAATTACTTGTGA	42	M2' Dock
CO-M-140	ATAACCGATCATCTTTGACCCCCAGCGATTATACCAAGTTCATGTTACTTAGCCGG	56	
CO-M-141	TGAGACTCGAGTTTCGTCACCAGTAGCCCTCATATGATGAAAGACTACC	49	
CO-M-142	GAACCACCATGCCCCCTGCCTATTTAAGAGGC	32	
CO-M-143	CCAGCAAAAGCCGCCACCCTCAGACGCCACCA	32	
CO-M-144	CGCAATAATAACGGAATATTCATTAAAGGTGAAATTAGAG	40	
CO-M-145	TCCCTCAGATCACCAGTAGCACCAAAATATTGTAGTACCGCAATAAGAG	49	
CO-M-146	GTAACACTCTCAAGAGAAGGATTAGGATTA	30	
CO-M-147	AGAATTTCGTAACGATCTAAAGTTCATGTACC	32	
CO-M-148	TAAAACACTATATTCGGTCGCTGATTTCGAGG	32	
CO-M-149	GGGAGTTAAACGAAAGAGGCGTCGCTCAACAGTAGGGCTTATCCAATCG	49	
CO-M-150	TTTCCAGACGGTTTATCAGCTTGCGGCTTGCA	32	
CO-M-151	AGGAGGTTGCCTTGAGTAACATAATTTAGGCAG	33	
CO-M-152	AGCAAGGCACCAGAGCCACCACCGGCATTGAC	32	

CO-M-153	AGACTCCTTTGAGGGAGGGAAGGTTTACCATT	32	
CO-M-154	TCAACCGATATTACGCAGTATGTTAGCAAACG	32	
CO-M-155	TCACCGGACGGAAACGTCACCAATGGCGACAT	32	
CO-M-156	GGGTCAGTGAGGCAGGTCAGACGAAATCAAAA	32	
CO-M-157	GGGATAGCGCTCAGTACCAGGCGGTTTTAACG	32	
CO-M-158	AATTGTATCGTTAGTAAATGAATTCATTTTCA	32	
CO-M-159	CAACCTAAAAGGCCGCTTTTGCGGGAGCCTTT	32	
CO-M-160	CCCTCAGCTACGTAATGCCACTACGAAGGCAC	32	
CO-M-161	GGGATTTTAAAAAGGCTCCAAAAGGATCGTCA	32	
CO-M-162	CGTCGAGATCAGAGCCACCACCCTTTCTGTAT	32	
CO-M-163	GATATTCAGTGTACTGGTAATAAGATAAGTGC	32	
CO-M-164	CGATAGCATTTGCCATCTTTTCATTTGGCCTT	32	
CO-M-165	TAGAAAATGCGCCAAAGACAAAAGGAAACCAT	32	
CO-M-166	GTTTACCAACATACATAAAGGTGGCAACATAT	32	
CO-M-167	TATTAGCGGCACCGTAATCAGTAGTTCATATG	32	
CO-M-168 [c]	ATACAGGACAAACAAATAAATCCTAGCCCCCT	32	
CO-M-169	CGCCACCCGGGTTGATATAAGTATTTTTGATG	32	
CO-M-170	TCTCCAAAGCTAAACAACTTTCAACTCAGAAC	32	
CO-M-171	GGGTAAAAAGCGAAAGACAGCATCGTTGAAAA	32	
CO-M-172	GGTAGCAATTCATGAGGAAGTTTCCATTAAAC	32	
CO-M-173	GCGGAGTGATAATAATTTTTTCACGGAACGAG	32	
CO-M-174 [B]	\5Biosg\ TTTTT ATAGGTGTCCTCAGAACCGCCACCCAGTTTCA	37	Biotin-labeled
CO-M-175 [B]	\5Biosg\ TTTTTTTTTT CCAGAATGAAGCGTCATACATGGCAGCCCGGA	42	Biotin-labeled
CO-M-176	TCAAGTTTCGGCATTTTCGGTCATCATTAAAG	32	
CO-M-177	AAAAGAAACACAATCAATAGAAAACGACAGAA	32	

Table S7 | Strand sequences for cross-shaped DNA origami tile (edge strands)

A-Tile Edge Strands

CO-A-D1*	CGTAACGTTAATATTTTGTTAATATTTAAATTGTAAAATACATCT	45	M1 dock/sticky-ends
CO-A-D2*	GTTCATGAGTAATGTGTAGGTTTTTAAATGCAATGCCATACATCT	45	M1 dock/sticky-ends
CO-A-D3*	TTTATTAGATACATTTCGCTAGATTTAGTTTGACCTTT	38	Blocking
CO-A-D4*	TTTATCAAAAAGATTAAGAAAGCAAAGCGGATTGCTTT	38	Blocking
CO-A-D5*	AGTGTATAACGCCAAAAGGAACAACTAATGCAGATACTGTAT	42	sticky-ends
CO-A-D6*	GACATGATATTCATTACCCAAATCTTGACAAGAACCGTGTAT	42	sticky-ends
CO-A-L1*	CGAATTCCTGAACAAGAAAAAATCAACAATAGATAAGATACATCT	45	M1 dock/sticky-ends
CO-A-L2*	AGCATTTGCACCCAGCTACAAAAGATTAGTTGCTATTATACATCT	45	M1 dock/sticky-ends
CO-A-L3*	TTTAATAATAAGAGCAAGAGAATTGAGTTAAGCCCTTT	38	Blocking
CO-A-L4*	TTTGTTTGAGGGGACGACGAACCGTGCATCTGCCATTT	38	Blocking
CO-A-L5*	GCAAACCCGGGTACCGAGGTCTCGACTCTAGAGGATCTGTAT	42	sticky-ends
CO-A-L6*	CTGTTAGCTGATTGCCCTTCACAGTGAGACGGGCAACTGTAT	42	sticky-ends
CO-A-R1	CTGTTGTTAAATAAGAATAAAGTGTGATAAATAAGGCTGTAT	42	sticky-ends
CO-A-R2	GCAAAAAATCGTCGCTATTAAATAACCTTGCTTCTGTTGTAT	42	sticky-ends
CO-A-R3	TTTAAATAAAGAAATTGCGTTAGCACGTAAAACAGTTT	38	Blocking
CO-A-R4	TTTTATTCCTGATTATCAGAGCGGAATTATCATCATTT	38	Blocking
CO-A-R5	AGCATTGCTGAACCTCAAATAATCTAAAGCATCACCTATACATCT	45	M1 dock/sticky-ends
CO-A-R6	CGAATACATTGGCAGATTCACCTGAAATGGATTATTTATACATCT	45	M1 dock/sticky-ends
CO-A-U1	GACATAATAAGTTTATTTTGTCGCAAAGACACCACGGTGTAT	42	sticky-ends
CO-A-U2	AGTGTTGTAGCGCGTTTTCATGCCTTTAGCGTCAGACTGTAT	42	sticky-ends
CO-A-U3	TTTAATTTACCGTTCCAGTGAAAGCGCAGTCTCTGTTT	38	Blocking

CO-A-U4	TTTGGTTTAGTACCGCCACATCACCGTACTCAGGATTT	38	Blocking
CO-A-U5	GTTCAACTAAAGGAATTGCGAAGAATAGAAAGGAACAATACATCT	45	M1 dock/sticky-ends
CO-A-U6	CGTAAGAGGACTAAAGACTTTCGGCTACAGAGGCTTTATACATCT	45	M1 dock/sticky-ends

B-Tile Edge Strands

CO-B-D1*	TTACGGTTAAATAAGAATAAAGTGTGATAAATAAGGCTGTAT	42	sticky-ends
CO-B-D2*	TGAACAAATCGTCGCTATTAAATAACCTTGCTTCTGTTGTAT	42	sticky-ends
CO-B-D3*	TTTAAATAAAGAAATTGCGTTAGCACGTAAAACAGTTT	38	Blocking
CO-B-D4*	TTTTATTCCTGATTATCAGAGCGGAATTATCATCATTT	38	Blocking
CO-B-D5*	ACACTTGCTGAACCTCAAATAATCTAAAGCATCACCTATACATCT	45	M1 dock/sticky-ends
CO-B-D6*	ATGTCACATTGGCAGATTCACCTGAAATGGATTATTTATACATCT	45	M1 dock/sticky-ends
CO-B-L1*	AACAGCGTTAATATTTTGTTAATATTTAAATTGTAAAATACATCT	45	M1 dock/sticky-ends
CO-B-L2*	TTTGCTGAGTAATGTGTAGGTTTTTAAATGCAATGCCATACATCT	45	M1 dock/sticky-ends
CO-B-L3*	TTTATTAGATACATTTCGCTAGATTTAGTTTGACCTTT	38	Blocking
CO-B-L4*	TTTATCAAAAAGATTAAGAAAGCAAAGCGGATTGCTTT	38	Blocking
CO-B-L5*	ATGCTATAACGCCAAAAGGAACAACTAATGCAGATACTGTAT	42	sticky-ends
CO-B-L6*	ATTCGGATATTCATTACCCAAATCTTGACAAGAACCGTGTAT	42	sticky-ends
CO-B-R1	ATTCGAATAAGTTTATTTTGTCGCAAAGACACCACGGTGTAT	42	sticky-ends
CO-B-R2	ATGCTTGTAGCGCGTTTTCATGCCTTTAGCGTCAGACTGTAT	42	sticky-ends
CO-B-R3	TTTAATTTACCGTTCCAGTGAAAGCGCAGTCTCTGTTT	38	Blocking
CO-B-R4	TTTGGTTTAGTACCGCCACATCACCGTACTCAGGATTT	38	Blocking
CO-B-R5	TTTGCACTAAAGGAATTGCGAAGAATAGAAAGGAACAATACATCT	45	M1 dock/sticky-ends
CO-B-R6	AACAGGAGGACTAAAGACTTTCGGCTACAGAGGCTTTATACATCT	45	M1 dock/sticky-ends
CO-B-U1	ATGTCTCCTGAACAAGAAAAAATCAACAATAGATAAGATACATCT	45	M1 dock/sticky-ends
CO-B-U2	ACACTTTGCACCCAGCTACAAAAGATTAGTTGCTATTATACATCT	45	M1 dock/sticky-ends
CO-B-U3	TTTAATAATAAGAGCAAGAGAATTGAGTTAAGCCCTTT	38	Blocking
CO-B-U4	TTTGTTTGAGGGGACGACGAACCGTGCATCTGCCATTT	38	Blocking
CO-B-U5	TGAACCCCGGGTACCGAGGTCTCGACTCTAGAGGATCTGTAT	42	sticky-ends
CO-B-U6	TTACGAGCTGATTGCCCTTCACAGTGAGACGGGCAACTGTAT	42	sticky-ends

Passivation Edge Strands

CO-A-R1 / B-D1	TTTGTTAAATAAGAATAAAGTGTGATAAATAAGGCTTT	38	Blocking
CO-A-R2 / B-D2	TTTAAATCGTCGCTATTAAATAACCTTGCTTCTGTTTT	38	Blocking
CO-A-R3 / B-D3	TTTAAATAAAGAAATTGCGTTAGCACGTAAAACAGTTT	38	Blocking
CO-A-R4 / B-D4	TTTTATTCCTGATTATCAGAGCGGAATTATCATCATTT	38	Blocking
CO-A-R5 / B-D5	TGCTGAACCTCAAATAATCTAAAGCATCACCTAATACATCT	41	M1 Dock
CO-A-R6 / B-D6	ACATTGGCAGATTCACCTGAAATGGATTATTTAATACATCT	41	M1 Dock
CO-A-D1 / B-L1	CGTTAATATTTTGTTAATATTTAAATTGTAAAAATACATCT	41	M1 Dock
CO-A-D2 / B-L2	TGAGTAATGTGTAGGTTTTTAAATGCAATGCCAATACATCT	41	M1 Dock
CO-A-D3 / B-L3	TTTATTAGATACATTTCGCTAGATTTAGTTTGACCTTT	38	Blocking
CO-A-D4 / B-L4	TTTATCAAAAAGATTAAGAAAGCAAAGCGGATTGCTTT	38	Blocking
CO-A-D5 / B-L5	TTTATAACGCCAAAAGGAACAACTAATGCAGATACTTT	38	Blocking
CO-A-D6 / B-L6	TTTGGATATTCATTACCCAATCTTCGACAAGAACCTTT	38	Blocking

Table S8 | Strand sequences for DNA-PAINT imager strands

Imager Strands

M1' - Cy3b	CTAGATGTAT/Cy3b/	10	M1' Imager Strand
M2' - Cy3b	ACTCACAAGT/Cy3b/	10	M2' Imager Strand

References

1. M. Ovesný, P. Křížek, J. Borkovec, Z. Svindrych and G. M. Hagen, *Bioinformatics*, 2014, **30,** 2389–90.

2. C. A. Schneider, W. S. Rasband and K. W. Eliceiri, *Nat. Methods*, 2012, **9,** 671–675.

3. R. E. Thompson, D. R. Larson and W. W. Webb, *Biophys. J.*, 2002, **82,** 2775–83.

4. M. Ovesny, PhD thesis, Charles University in Prague, 2016, <https://www.researchgate.net/publication/311426573_Computational_methods_in_single_molecule_localization_microscopy>